



TAMPEREEN TEKNILLINEN YLIOPISTO  
TAMPERE UNIVERSITY OF TECHNOLOGY

Heikki Virtanen

**Narrow-Linewidth DFB and DBR Lasers with Surface  
Gratings Fabricated Using UV-Nanoimprint Lithography**



Julkaisu 1512 • Publication 1512

Tampereen teknillinen yliopisto. Julkaisu 1512  
Tampere University of Technology. Publication 1512

Heikki Virtanen

## **Narrow-Linewidth DFB and DBR Lasers with Surface Gratings Fabricated Using UV-Nanoimprint Lithography**

Thesis for the degree of Doctor of Science in Technology to be presented with due permission for public examination and criticism in Sähkötalo Building, Auditorium S2, at Tampere University of Technology, on the 24th of November 2017, at 12 noon.

Tampereen teknillinen yliopisto - Tampere University of Technology  
Tampere 2017

Doctoral candidate: Heikki Virtanen, M. Sc  
Optoelectronics Research Centre  
Faculty of Natural Sciences  
Tampere University of Technology  
Finland

Supervisor: Jukka Viheriälä, Doc.  
Optoelectronics Research Centre  
Faculty of Natural Sciences  
Tampere University of Technology  
Finland

Instructor: Mircea Guina, Prof.  
Optoelectronics Research Centre  
Faculty of Natural Sciences  
Tampere University of Technology  
Finland

Pre-examiners: Edik Rafailov, Prof.  
Aston Institute of Photonic Technologies  
Aston University  
United Kingdom

Harri Lipsanen, Prof.  
Department of Electronics and Nanoengineering  
Aalto University  
Finland

Opponent: Trevor Hall, Prof.  
School of Electrical Engineering and Computer Science  
University of Ottawa  
Canada

# Abstract

This thesis presents the design, modeling, and fabrication of high performance narrow-linewidth edge-emitting semiconductor distributed feedback (DFB) and distributed Bragg reflector (DBR) lasers employing surface gratings fabricated without epitaxial re-growth. The re-growth free fabrication method mitigates the risks of contamination and atmospheric oxidization in the active and waveguide layers, improving the device performance, reliability and yield. Compared to conventional buried gratings, in the surface gratings the injected carriers have much less interaction with the defect prone processed interfaces, which decreases the non-radiative recombination and the probability of degradation, increasing the reliability, particularly at high injection currents.

In this work soft-stamp ultraviolet (UV)-nanoimprint lithography (NIL) has been used to define the etch masks. Unlike in conventional photolithography, the UV-NIL's resolution is not limited by diffraction and scattering effects. Moreover, UV-NIL has low fabrication costs and high throughput, which makes it ideal for a large scale mass production.

The thesis discusses how the device design can influence the emission linewidth and how this affects other laser characteristics, some of which require contradictory design parameters. For example a decreasing mirror loss reduces the linewidth but also reduces the slope efficiency, limiting the maximum output power. Also novel device design elements have been introduced to alleviate the technological limitations of the fabrication process. A laterally coupled (LC)-ridge waveguide (RWG) grating with lateral protrusions alternating on the sides of the central ridge has been employed to enable the fabrication of gratings having wider trenches than the grating period and reduced lateral current leakage. Under the technological restrictions given by the achievable etching aspect ratio, the wider trenches enable the fabrication of lower order gratings, reducing radiation losses.

The fabricated devices achieved state-of-the-art characteristics: 30 mW to 40 mW output power with  $\sim 10$  kHz full width at half maximum (FWHM) linewidths at 300 mA bias current for 780 nm DFB lasers and  $\sim 500$  mW output power with  $< 250$  kHz FWHM linewidths at 1630 mA bias current for 1180 nm DBR lasers. Also monolithic master oscillator power amplifier (MOPA) lasers have been fabricated to avoid the compromise between achieving a narrow linewidth and a high power as well as to enable independent control of the emission wavelength and output power.  $\sim 7$  W output power was obtained for a 780 nm MOPA laser with a 3 mm long DFB master oscillator (MO) section and a 4 mm long tapered power amplifier (PA) section under 500 mA continuous wave (CW)-mode bias for the MO section and 15 A pulsed-mode bias (1  $\mu$ s pulse width and 1% duty cycle) for the PA section. The pulsed-mode operation of the PA section, which did not enable accurate emission linewidth measurement for the MOPA lasers, was employed because the p-side up mounting did not provide good enough thermal management.





# Preface

This thesis outlines the work carried out by its author with the modeling, design, and device fabrication at Optoelectronic Research Centre (ORC), Tampere University of Technology. I gratefully acknowledge the financial support of the European Space Agency (ESA) and the Finnish Funding Agency of Technology and Innovations (TEKES).

It has been a great privilege to work at ORC. I wish to thank the entire personnel of ORC. Particularly, I want to thank my former supervisor Dr. Docent Mihail Dumitrescu and my colleagues MSc. Topi Uusitalo and MSc. Antti Aho for all the help, encouragement, cooperation, support and discussions that they have provided during these years when I have worked at ORC. I want to thank my supervisor Dr. Jukka Viheriälä for his help and support. I am also grateful to my instructor Prof. Mircea Guina who made possible the completion of this thesis at ORC. I want to extend my gratitude to all the people in the supporting staff, including MSc. Mervi Koskinen, Mariia Bister, Maija Karjalainen, MSc. Heidi Tuorila and MSc. Jarno Reuna. Without them many of the research objectives of this study could not have been reached. Moreover, I wish to thank Dr. Sanna Ranta who has grown most of the epiwafer materials used in this study, and MSc. Joel Salmi who taught me how to process edge-emitting semiconductor lasers and how to use all those weird looking equipment in the clean room facilities of TUT.

Finally, I would like to thank my parents, my brother, and friends for their moral support over the years.

Tampere, November, 2017

Heikki Virtanen

# Contents

<b>Abstract</b>	<b>i</b>
<b>Preface</b>	<b>iii</b>
<b>Contents</b>	<b>iv</b>
<b>Acronyms</b>	<b>vii</b>
<b>Nomenclature</b>	<b>ix</b>
<b>List of Publications</b>	<b>xi</b>
<b>Author's contribution</b>	<b>xiii</b>
<b>1 Introduction</b>	<b>1</b>
1.1 Research objectives and scope of the thesis . . . . .	2
<b>2 Grating structures</b>	<b>7</b>
<b>3 Lithography techniques</b>	<b>9</b>
3.1 Electron beam lithography . . . . .	9
3.2 Optical lithography . . . . .	10
3.3 Nanoimprint lithography . . . . .	11
<b>4 Design of narrow-linewidth DFB and DBR lasers</b>	<b>15</b>
4.1 Linewidth theory . . . . .	15
4.1.1 External linewidth broadening . . . . .	18
4.2 DFB and DBR lasers . . . . .	19
4.3 Transverse and epilayer structures . . . . .	22
4.4 Longitudinal structure . . . . .	25
4.5 Master oscillator power amplifier laser structure . . . . .	30
<b>5 The fabrication of DFB and DBR lasers with surface gratings using soft stamp UV-nanoimprint lithography</b>	<b>33</b>
5.1 Epitaxial growth . . . . .	33
5.2 Post-growth rapid thermal annealing . . . . .	34
5.3 LC-RWG grating fabrication stages . . . . .	35
5.3.1 Soft stamp fabrication . . . . .	35
5.3.2 UV-nanoimprint and lift-off . . . . .	35
5.3.3 Grating etching . . . . .	36

---

5.4	Planarization and contact openings . . . . .	38
5.5	p- and n-side metalization . . . . .	39
5.6	Dicing and mounting . . . . .	39
5.7	Fabrication limitations . . . . .	40
<b>6</b>	<b>Device characterization results</b>	<b>45</b>
6.1	DFB characterization results . . . . .	45
6.2	DBR characterization results . . . . .	52
6.3	MOPA characterization results . . . . .	54
<b>7</b>	<b>Conclusions</b>	<b>57</b>
<b>8</b>	<b>Appendix A</b>	<b>61</b>
	<b>Bibliography</b>	<b>63</b>
	<b>Publications</b>	<b>71</b>



# Acronyms

**AR** anti-reflection

**ARDE** aspect ratio dependent etching

**ASE** amplified spontaneous emission

**BCB** benzocyclobutene

**CDSPST** contrast difference between the second peak and the second trough

**CHF<sub>3</sub>** trifluoromethane

**CMP** chemical mechanical polishing

**CW** continuous wave

**DBR** distributed Bragg reflector

**DFB** distributed feedback

**EBL** electron beam lithography

**ESA** electronic spectral analyzer

**ET** etched through

**FIB** focused ion beam

**FP** Fabry-Perot

**FWHM** full width at half maximum

**HR** high-reflection

**ICP-RIE** inductively coupled plasma reactive ion etching

**LC** laterally coupled

**LD** laser diode

**LI** light-current

**LIV** light-current-voltage

**MBE** molecular beam epitaxy

**MO** master oscillator

**MOPA** master oscillator power amplifier  
**mr-UVCur06** UV-curable nanoimprint resist  
**NaClO** sodium hypochlorite  
**NIL** nanoimprint lithography  
**NMP** n-methyl pyrrolidone  
**OL** optical lithography  
**ORC** Optoelectronic Research Centre  
**OSA** optical spectrum analyzer  
**PA** power amplifier  
**PDMS** polydimethylsiloxane  
**PIC** photonic integrated circuit  
**PL** photoluminescence  
**PMGI** polymethylglutarimide  
**PS** phase shift  
**PSD** power spectral density  
**QW** quantum well  
**RIE** reactive-ion etching  
**RWG** ridge waveguide  
**SCH** separate confinement heterostructure  
**SEM** scanning electron microscope  
**SF<sub>6</sub>** sulfur hexafluoride  
**SHB** spatial hole burning  
**SiO<sub>2</sub>** silicon dioxide  
**SMSR** side mode suppression ratio  
**SOA** semiconductor optical amplifier  
**TDTW** time domain traveling wave  
**TE** transverse electric  
**TiO<sub>2</sub>** titanium dioxide  
**TM** transverse magnetic  
**UV** ultraviolet  
**VCSEL** vertical cavity surface emitting laser  
**VI** voltage-current

# Nomenclature

$\alpha$  amplitude ratio of the interfering optical fields

$\alpha_H$  linewidth enhancement factor

$\alpha_i$  intrinsic/internal loss factor

$\alpha_m$  mirror loss factor

$c$  speed of light in vacuum

$N$  carrier density

$D$  lateral extension of the grating protrusions

$\delta$  delta function

$\Delta f$  spectral separation between the interference minima

$E_0$  optical field amplitude

$\eta_i$  internal quantum efficiency

$F$  time averaged total photon number coupled to the lasing mode in the laser cavity

$g$  etch depth

$h$  Planck constant

$I$  bias current

$I_{th}$  threshold bias current

$\kappa \cdot L$  coupling strength

$\lambda$  emission wavelength

$\Lambda_1$  grating protrusion width (in the longitudinal direction)

$\Lambda_2$  grating trench width

$L_{\text{coh}}$  coherence length

$L_{\text{fiber}}$  fiber length

$n$  refractive index

$n_{\text{eff}}$  effective refractive index



$n_{sp}$  spontaneous emission factor

$N_{th}$  threshold carrier density

$\Delta\nu$  laser linewidth

$\nu$  optical frequency

$\Omega$  modulation frequency of the acousto-optic modulator

$P_0$  output power per facet

$K_c$  Petermann factor

$q$  elementary charge

$R_{sp}$  time-averaged total spontaneous emission rate in the laser cavity

$S_0$  linewidth parameter

$t$  thickness of the remaining un-etched cladding

$\tau_c$  carrier lifetime

$\tau_{coh}$  coherence time

$\tau_{delay}$  time delay between the interfering optical fields

$V$  potential difference between the quasi-Fermi levels

$V_{act}$  active region volume

$v_g$  group velocity

$W$  central ridge width

# List of Publications

- Pub1 H. Virtanen, T. Uusitalo, and M. Dumitrescu, "Simulation studies of DFB laser longitudinal structures for narrow linewidth emission", *Optical and Quantum Electronics*, vol. 49, no. 4, pp. 160, 2017
- Pub2 H. Virtanen, A. T. Aho, J. Viheriala, V.M. Korpijarvi, T. Uusitalo, M. Koskinen, M. Dumitrescu, and M. Guina, "Spectral characteristics of narrow linewidth high-power 1180 nm DBR laser with surface gratings", *IEEE Photonics Technology Letters*, vol. 29, no. 1, pp. 114–117, 2017
- Pub3 H. Virtanen, T. Uusitalo, M. Karjalainen, S. Ranta, J. Viheriala, and M. Dumitrescu, "Narrow-linewidth 780 nm DFB laser fabricated using nanoimprint lithography", *IEEE Photonics Technology Letters*, – Approved
- Pub4 T. Uusitalo, H. Virtanen, M. Karjalainen, S. Ranta, J. Viheriala, and M. Dumitrescu, "Distributed feedback lasers with alternating laterally-coupled ridge-waveguide surface gratings", *Optics Letters*, vol. 42, no. 16, pp. 3141–3144, 2017



# Author's contribution

This thesis includes 3 papers that are already published in international scientific journals and 1 submitted publication. All 4 publications are generated from the results of the author's research studies and from author's collaboration with other scientists. The work presented in the thesis comprises modeling, simulation, design, fabrication and characterization of edge-emitting semiconductor DFB and DBR lasers.

Publication [Pub1] deals with the modeling, simulation and design of semiconductor DFB lasers, particularly aiming for achieving high-power narrow linewidth emission through variations in the longitudinal structure of the devices. For this study, the thesis author developed the Time-Domain Traveling-Wave model, carried out the numerical simulations and analytic evaluations and took the main responsibility in the publication process.

Publication [Pub2] demonstrates high-power narrow-linewidth 1180 nm DBR lasers with surface gratings fabricated using soft-stamp UV-NIL. In Publication [Pub2] the thesis author contributed to the device processing and characterization, performing the light-current-voltage (LIV) and linewidth measurements that were essential parts of the study. Moreover, in Publication [Pub2] the author wrote the main parts of the publication.

Publication [Pub3] demonstrates narrow-linewidth 780 nm DFB lasers with LC-RWG surface gratings, while publication [Pub4] presents a comparison between 780 nm DFB lasers with LC-RWG surface gratings having the lateral protrusions placed either symmetrically on both sides or alternately on one and on the other side of the central ridge. For Publications [Pub3] and [Pub4] the thesis author assisted in the design of the lasers, particularly dealing with the longitudinal aspects of the structures, and carried out the structural characterization. In addition, for both these publications, the thesis author processed himself, coordinated, supervised, or closely co-operated with the person who carried out various process steps. Furthermore, in Publication [Pub3], the thesis author contributed to the device characterization, performed linewidth fittings and data processing that were a crucial part of the publication, wrote most of the paper and organized the publication. In Publication [Pub4] the manuscript writing was split between the thesis author and Topi Uusitalo.

Topi Uusitalo is the main co-author of the publications included in this thesis and the first author of publication [Pub4], which is also included in Topi Uusitalo's doctoral dissertation. Topi Uusitalo contributed to transverse structure modeling, simulation and design for all publications while the thesis author contributed to the longitudinal structure modeling, simulation and design for all publications. Also in all papers the thesis author contributed to the device processing and structural characterization while Topi Uusitalo contributed to the development of characterization setups. In Publication [Pub4] Topi Uusitalo carried out the simulation studies and took the main responsibility of the characterization work, including the LIV and spectral measurements. He also contributed

to publications [Pub1] and [Pub3] by editing the manuscripts. For Publication [Pub2] he built the delayed self-homodyne linewidth measurement system and for Publication [Pub3] Topi Uusitalo conducted the delayed self-heterodyne linewidth measurements.

Mihail Dumitrescu developed the epilayer structures, coordinated the modeling, simulation, design and laser structure development work and coordinated the writing and editing of all publications.

Mircea Guina organized the research work in [Pub2]. He also edited the final version of the [Pub2] manuscript. Sanna Ranta ([Pub3], [Pub4]) and Ville-Markus Korpijärvi ([Pub2]) grew the epiwafers from which the reported devices were fabricated. Mervi Koskinen ([Pub2]) and Maija Karjalainen ([Pub3], [Pub4]) contributed to the device processing.

Jukka Viheriälä coordinated the process development and Antti Aho drew the process masks that were used in the device fabrication.

# 1 Introduction

Today lasers are very present in our everyday lives in many ways, sometimes unnoticed. We see them in laser scanners and in robot welding on assembly lines, but lasers are also used in medical applications [1], to measure distances [2], to transfer information from one place to another [3], and to provide atomic frequency standards [4]. Lasers are employed in sensors and in spectroscopy applications to measure the presence and concentrations of different elements, gases or compounds [5] and are also used to solve fundamental physics problems [6]. The huge number of laser applications is ever increasing. This rapid development is accompanied by more stringent requirements for the lasers. Multiple applications require that the laser is very reliable and efficient, while providing high spectral purity and high output power (e.g. the optical frequency standards and the precision spectroscopy need lasers that have a lifetime over many years with less than 100 kHz free-running emission linewidth and emitting a few tens of milliwatts of optical power [4, 7]). Such requirements are usually very challenging to fulfill simultaneously, particularly, if the laser source must also be compact, mechanically robust, and tolerant with respect to other external perturbations.

Laser diodes (LDs) (i.e. semiconductor lasers) can satisfy most of the requirements mentioned above. LDs also possess many other properties such as an adjustable emission wavelength and high direct modulation speed. Moreover, LDs are user-friendly in the sense that their input voltages and currents are relatively low, they require very minimal or no maintenance, and they are relatively easy to incorporate with photonic integrated circuits (PICs).

Even though semiconductor lasers can fulfill many requirements, these devices have also restrictions and limitations. In many applications the most crucial limitations are the phase and intensity noise levels of LDs. In general commercial free-running LDs have higher noise levels at a given frequency than for example typical large, more expensive, and less efficient solid state or fiber lasers [8]. These limitations of LDs are inherent due to the strong coupling of phase and intensity noises in semiconductor lasers [9]. Therefore, in order to minimize the spectral width and to simultaneously obtain a relatively high power level, a good beam quality and a long device lifetime, the device structure and fabrication must be carefully designed.

There are several types of LDs that have been used to achieve a narrow emission linewidth such as vertical surface emitting lasers (VCSELs), and DFB and DBR edge emitting lasers. VCSELs emit light in the vertical direction of the chip surface. Due to the short effective length of the device cavity, VCSELs have a small active region volume, low saturated output power, and a relatively broad emission linewidth compared to typical DFB lasers [10]. VCSELs are also sensitive to temperature variations [10], which limits their operation temperature range drastically. Edge emitting DFB and DBR lasers have

much longer cavities and larger active region volumes that enable higher output powers and narrower linewidths [11, 12]. Consequently, this thesis considers edge emitting DFB and DBR lasers that can be utilized in many applications requiring narrow linewidth with a relatively high power level and a good beam quality.

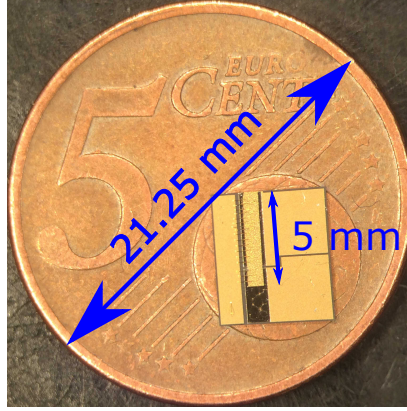


**Figure 1.1:** Picture of a p-side down mounted DFB MOPA laser with surface gratings on top a 5 cent coin.

The thesis includes six more chapters. Chapter 2 briefly presents the surface gratings and their particularities and advantages, Chapter 3 discusses the main lithography techniques and the advantages of employing ultra-violet nanoimprint lithography in the fabrication process. Chapter 4 introduces the fundamental theory governing the semiconductor laser linewidth and discusses the properties and particularities of DFB and DBR lasers with index coupled surface gratings. The chapter analyzes what is required from the laser structure to obtain a narrow emission linewidth and what device parameters affect the spectral and other characteristics such as output power. The epilayer, transverse and longitudinal structures are considered in this chapter. The chapter also presents simulation and optimization studies of DFB and DBR lasers.

Chapter 5 describes in detail the fabrication of narrow linewidth DFB and DBR lasers using soft stamp UV-NIL. The chapter presents the fabrication process flow from template fabrication and template replication onto soft stamp to imprint, lift-off and etching of the surface gratings. The chapter also describes all the process steps in the device fabrication and discusses the fabrication limitations.

Chapter 6 presents laser characterization results emphasizing the linewidth measurement results. The chapter provides the descriptions of the used measurement systems and discusses the results. Chapter 7 presents a short summary of the results, gives the conclusions and outlines future research directions.

## 1.1 Research objectives and scope of the thesis

This thesis is focused on the modeling, design, fabrication and characterization of low cost edge-emitting narrow linewidth 780 nm DFB LDs with laterally-coupled ridge-waveguide (LC-RWG) surface gratings and 1180 nm DBR LDs with etched through (ET)-RWG surface gratings. The thesis describes and investigates the particularities of the LC-RWG DFB and of the ET-RWG DBR laser structures and analyzes the possibilities to achieve

high performances, particularly with respect to achieving a narrow linewidth emission and a high output power. The target of achieving a low cost for the developed lasers, which is required by many applications, has been addressed by developing a cost-effective high-throughput fabrication method, which employs soft stamp UV-NIL for defining the surface grating features and is suitable for mass-production.

The fabricated lasers target fulfilling the linewidth and output power requirements of applications in which moderate optical power levels (20 mW to 500 mW) and narrow linewidths (<100 kHz to 500 kHz) are needed. For applications requiring higher output powers and independent control of the emission wavelength and of the output power, the thesis also introduces MOPA laser structures that can provide high output power (>1 W) and narrow emission linewidth (<100 kHz to 250 kHz) simultaneously.

The lasers developed in this thesis can have various applications, including different frequency standards (particularly rubidium atomic clocks which are the primary target for the lasers emitting at 780 nm in this thesis), sensors, high speed wide bandwidth (coherent) optical communication links, LiDAR (e.g. for terrestrial mapping), spectroscopy and biomedical applications (the 1180 nm lasers developed in this thesis are addressing biomedical applications at 590 nm with frequency doubling). The linewidth and output power requirements for some of the most important applications are given in Table 1.1.

**Table 1.1:** Output power and linewidth requirements for some applications of narrow linewidth semiconductor lasers

Application	Wavelength (nm)	Linewidth (kHz)	Power (mW)	Special demands
Frequency standards	(Sr) 461, (Ca) 657, (Rb) 780, (Cs) 894 <sup>b</sup>	150-500 [4, 13]	2-50 <sup>a</sup> [4, 13]	long term amplitude and frequency stability
Communication	1310, 1550	10-100 <sup>c</sup> [15, 16]	1–10 [16, 17]	high efficiency, high beam quality
Atomic spectroscopy	many different wavelengths	80-250 [18–20]	50-200 [18–20]	wide mode-hop-free wavelength tuning range
Biomedical applications	many wavelengths including 590 nm	<sup>d</sup>	1-10 W	high power, good beam quality

<sup>a</sup>Fountain atomic clocks can require lasers with the output power levels in the range of 1 W with an intrinsic free-running linewidth of a few hundred kilohertz [14].

<sup>b</sup>Only the main target wavelength and the associated linewidth and output power ranges have been considered for each of the atomic clocks based on different atoms/ions, although the atomic clocks require multiple lasers at different wavelengths (e.g. for cooling in several stages, re-pumping, quenching, probing). The linewidth and power requirements vary depending on the use of the laser in the atomic clock, with secondary cooling and probing lasers having the most stringent linewidth requirements.

<sup>c</sup>Modern coherent optical communication systems require linewidth and symbol rate products in the range of  $10^{-2}$ – $10^{-5}$ .

<sup>d</sup>A narrow linewidth is required to improve the second harmonic generation efficiency; usually the medical applications themselves do not require narrow linewidths.

In order to reach stable single mode emission with narrow linewidth and a relatively high power, the developed 780 nm DFB and 1180 nm DBR device structures require extensive optimization. The device optimization has addressed all the parameters that can be adjusted by design and influence the emission linewidth:

- the internal and mirror losses
- the linewidth enhancement factor



- the Petermann factor
- the injection efficiency
- the active region volume
- the grating dimensions (etching depth, ridge width, lateral extension of the LC-RWG grating protrusions)
- the grating coupling coefficient
- the grating length

The optimizations targeting narrow emission linewidth have also taken into account the influences on other laser characteristics as well as the technological restrictions imposed by the fabrication process. Epilayer structure, doping profile and device structure optimizations were used to reduce the internal losses and to increase the injection efficiency. The mirror losses were reduced by appropriately choosing the grating coupling coefficient and the grating length. The linewidth enhancement factor was reduced by red-shifting the gain peak with respect to the grating Bragg resonance, which increased the differential gain. Single quantum well (QW) active regions have been used since they have a smaller volume and a lower threshold current than multi-QW structures at low total loss levels (which are also targeted for achieving narrow linewidth emission). The grating dimensions have been optimized to enable a high modal discrimination in favor of the fundamental transverse mode and to provide the target coupling coefficient. The gratings have been designed to have a relatively low coupling coefficient ( $\kappa$ ) to prevent highly non-uniform longitudinal photon and carrier density distributions, which are associated with longitudinal spatial hole burning that cause linewidth re-broadening. Long gratings (in the 1-3 mm range) have been employed to enable reasonably high grating strengths ( $\kappa \cdot L$ ), good optical feedback and low mirror losses.

Table 1.2 shows a comparison between widely used lithography techniques that can be used to fabricate DFB and DBR lasers. The table indicates clearly that UV-NIL, which has low fabrication costs, high resolution (e.g. a short grating pitch) and high throughput, is better suited for large scale mass production than electron beam lithography (EBL) or optical lithography (OL). Moreover, UV-NIL is as flexible as EBL enabling to define extremely complex device structures without any periodicity requirements. Due to these reasons, UV-NIL has been chosen for the fabrication of the devices reported in this thesis.

**Table 1.2:** A comparison of different lithography techniques.

Lithography type	Resolution	Capital cost	Operation cost	Throughput	Flexibility
Electron beam	high	high	high	very low	high
Optical	low <sup>a</sup>	low	low	high	high/low <sup>b</sup>
UV-nanoimprint	high	low	low	high	high

<sup>a</sup>Resolution enhancement techniques can be used to improve the resolution but these techniques also increase the system costs.

<sup>b</sup>Interference lithography can obtain a high resolution with low costs but this technique allows to fabricate periodic structures only.

The thesis presents the whole fabrication flow (including the UV-NIL lithography) of DFB and DBR lasers with surface gratings, including structures with an integrated

semiconductor optical amplifier (SOA) section. The limitations of the fabrication flow are identified and it is pointed out that the surface grating etching gives the most stringent limitations in the fabrication of the considered laser structures and in achieving the target structural dimensions.

Furthermore, the thesis shows that there are several restrictions and trade-offs in the design of the lasers with surface gratings. A deeper grating etching depth improves the coupling coefficient, improves the lateral optical confinement (for LC-RWG gratings), and influences the gain-loss discrimination of higher order transverse modes. However, since etching into the p-side waveguide layer has detrimental effects on the laser characteristics while the etching depth accuracy in the absence of an etch-stop layer is about  $\sim 50\text{--}100\text{ nm}$ , the thickness of the unetched cladding is usually in the range of  $0\text{--}200\text{ nm}$ . A longer lateral extension ( $D$ ) of the LC-RWG grating protrusions increases the coupling coefficient and enables better etching profile, but at the same time it increases the lateral current spreading. Hence, taking into account that the coupling coefficient increase typically saturates for  $D$  above  $2.5\text{ }\mu\text{m}$ , the lateral extension of the LC-RWG grating protrusions is in the range of  $D=0.5\text{--}2.5\text{ }\mu\text{m}$ . A wider central ridge reduces the series resistance and increases the saturated output power, but reduces the coupling coefficient and promotes higher order transverse modes. Also the lower bound of the central ridge width is technologically limited by the alignment accuracy of the contact openings. Thus, the central ridge width is typically in the range of  $1.0\text{--}3.0\text{ }\mu\text{m}$ .

The surface grating etching is limited by the etch aspect ratio (i.e. the ratio between the etching depth and the etched trench width) and it is very difficult to obtain good etching profiles with aspect ratios larger than 10. Since the etching depth target is usually close to the p-side waveguide layer, at a depth of  $1\text{--}1.25\text{ }\mu\text{m}$  corresponding to the thickness of the epilayers grown on top of the p-side waveguide, it is very difficult to etch gratings with trench widths below  $\sim 100\text{ nm}$ . This limitation affects the choices of grating orders and filling factors in surface grating structures at a given wavelength. A novel LC-RWG grating structure with alternating lateral protrusions has been demonstrated to alleviate the etch aspect ratio limitation and enable the fabrication of short visible wavelength DFB lasers with low-order LC-RWG gratings.



## 2 Grating structures

Although LDs are inexpensive compared to many other types of lasers, high performance narrow linewidth ( $< 1$  MHz) semiconductor lasers are still too expensive for many applications because the device structures require a feedback mechanism that supports only a single narrow linewidth oscillating mode in the laser cavity and strongly suppresses all the other modes. Such a feedback structure can be implemented in various ways [21, 22], but a grating structure is often employed.

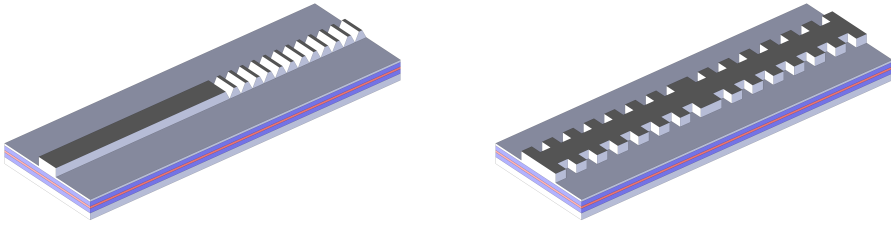
Traditionally two different grating types have been used for DFB and DBR lasers: buried or surface gratings. The fabrication of buried gratings needs at least two epitaxial growth steps since the growth must be interrupted and the buried grating structure must be processed before the rest of the epilayer structure is epitaxially overgrown. Despite the fact that the device structures are protected most of the time while being processed, the processing introduces crystalline imperfections on the processed surfaces and the processed interfaces are exposed to contamination, even if for a short period of time. Moreover, aluminum containing processed surfaces are susceptible to oxidation, which can introduce detrimental defects to the structure. All these crystalline defects, contaminations and oxidations can act as centers for non-radiative recombination and photon absorption events that ultimately degrade the device performance and the lifetime [23].

The surface gratings circumvent the problems caused by the overgrowth. For surface gratings, the feedback structure is etched into the cladding of the epitaxial growth step has been completed. Thus, the fabrication is simplified (reducing the fabrication costs and increasing the throughput) and the defect-prone processed interfaces are kept away from the carrier flow and from regions with high optical field intensity and high temperature. Placing the inherent processing related defects away from critical regions in the structure improves the laser characteristics, reduces the degradation during operation (and the associated characteristics' drift) and improves the laser reliability.

There are different types of surface grating structures that have been applied for LDs, including LC metal and semiconductor surface gratings. LC metal gratings are formed on the sides of the RWG structure perpendicular to the ridge that provides the lateral confinement [24]. Due to the optical absorption in metals, the presence of the metal gratings is associated with complex coupling (i.e. longitudinally periodic loss variation). Although the metal gratings' complex coupling provides longitudinal mode selection, the associated losses affect the laser performances. The LC-RWG semiconductor gratings employ lateral corrugations etched into the sides of the RWG [25, 26], which are mainly associated with index coupling (i.e. longitudinally periodic variation of the real part of the effective refractive index). Because the metal gratings introduce supplementary optical absorption losses, the output power of lasers that use complex coupled gratings is typically lower as compared to lasers that employ index coupled semiconductor gratings

etched into the sides of the RWG. Also the stability of single longitudinal mode operation under high pumping is reduced for the lasers with metal gratings. In this work, only the index coupled semiconductor surface gratings are investigated.

Unlike DFB lasers, where the gain and feedback occur together along the laser cavity, DBR lasers employ spatially separate gain and feedback sections, which enable the use of un-pumped passive high contrast semiconductor DBR mirrors etched through the RWG. The DBR lasers can typically achieve higher output powers than DFB lasers. Also the high effective refractive index contrast can give a high reflectivity with a shorter grating length but it also impairs the possibility to achieve a very narrow emission linewidth. Moreover, although in both DFB and DBR lasers the emission wavelength tuning is associated with a variation of the output power (in DBR lasers because the emission wavelength tuning is typically achieved by changing the bias of the gain section), the emission wavelength tuning range of the DBR lasers is smaller than the emission wavelength tuning range of the DFB lasers.



DBR laser with ET-RWG surface gratings.    A quarter wave shifted DFB laser with LC-RWG surface gratings-

**Figure 2.1:** Sketches of DBR and DFB lasers with surface gratings. The sketches illustrate the device structures after the surface gratings have been etched, without the subsequent fabrication steps.

## 3 Lithography techniques

As mentioned in the previous chapter, surface gratings can be fabricated easier (without overgrowth) and with lower costs than buried gratings. This is valid particularly when a reliable, accurate, high throughput, low cost lithography technique can be used to create the pattern of the surface gratings on a stable polymer. This patterned polymer layer can protect/mask some areas of the underlying semiconductor epilayer structure from the etchant in dry or wet etching. Alternatively, a patterned polymer layer can be used as a sacrificial layer in the fabrication of a metal etch mask using a lift-off process.

In this section three techniques that have typically been applied to pattern polymer or other material layers on a semiconductor surface (EBL, OL and nanoimprint lithography (NIL)), are discussed and their benefits and disadvantages are analyzed.

### 3.1 Electron beam lithography

EBL was used to define the grating structures in the early DFB lasers with surface gratings. In EBL the sample surface is covered with a layer of an electron beam sensitive polymer (i.e. resist), which is exposed to a focused electron beam after the excess solvent is removed by baking. The pattern features are written by the electron beam on the resist. After the exposure to the electron beam the resist becomes soluble or insoluble (depending on its chemical properties) in a special solution called developer. Therefore by exposing only some areas of the resist to the electron beam and dissolving the soluble areas, the desired pattern can be engraved on the resist layer. The stages of the electron beam lithography process are illustrated in Figure 3.1.

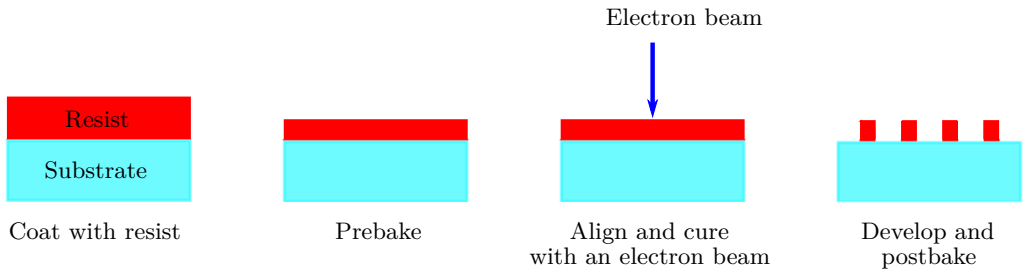


**Figure 3.1:** Stages of the electron beam lithography process.

Due to the extremely short electron wavelength, the theoretical resolution that can be obtained with the focused electron beam is very high. However, the practical resolution of EBL is not diffraction-limited but is limited by electron scattering in the resist and

by other process steps [27]. The long range accuracy of EBL may suffer from stitching errors because large patterns are split into small blocks that are within the maximum electron beam deflection range. Once a block is written by the electron beam, the sample is moved using a high resolution mechanical stage and any inaccuracy in the movement of the stage combined with thermal drift can induce stitching errors in large patterns [28].

The use of the maskless electron beam lithography technique becomes impractical and costly for large scale laser production because the very small beam spot size has to be serially scanned over the whole area of the underlying epiwafer and the exposure times are very long for large areas including hundreds or even thousands of lasers per epiwafer. Parallel EBL systems can mitigate the low throughput, but the availability and the costs of massively parallel EBL systems still limits the use of these instruments [29].

### 3.2 Optical lithography

The optical lithography is a technique that has been used starting from the early days of integrated electronic circuits. This lithography technique is still widely used due to its simplicity, low costs, and high throughput.

In OL the sample surface is coated with a thin layer of photosensitive chemical/polymer called photoresist mixed with a solvent. After most of the solvent is evaporated in the prebake, the photoresist layer is exposed to light with intensity variations, which changes the chemical properties of the photoresist, turning the exposed resist either soluble or insoluble to a developer. In industrial applications the exposure intensity variation is typically created by a mask with transparent and opaque areas. By dissolving the soluble areas of the resist layer, the intensity variations of light are transfered on the photoresist, which is then hardened in the postbake. In the following steps, the remaining hardened photoresist can be used as a protection layer for structures beneath it during subsequent wet or dry etching into the sample surface. The stages of the OL process are illustrated in Figure 3.2.

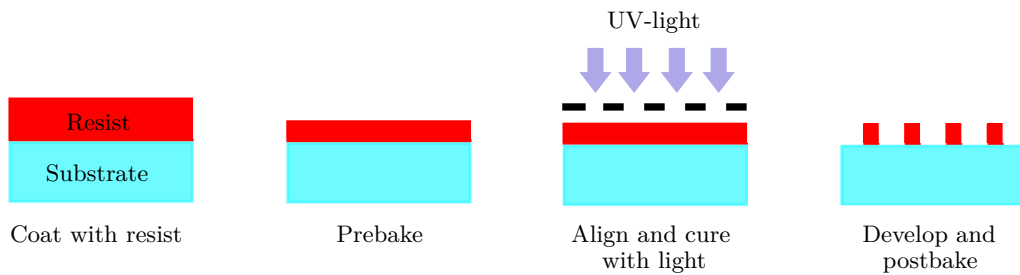


**Figure 3.2:** Stages of the optical lithography process with a positive UV-resist.

OL is much faster, simpler and cheaper than EBL by defining the patterns over the whole epiwafer in parallel with much less complex equipments. However, contact OL is capable of much lower resolution than EBL since the diffraction limit, which sets the fundamental physical limitation for the resolution, is proportional to the wavelength of the irradiating light source and inversely proportional to the numerical aperture of the illumination system. Therefore, light sources with shorter emission wavelengths and photoresists compatible for these shorter wavelengths have been developed to fabricate

smaller features using OL [30]. On the other hand shorter illumination wavelengths lead to technical difficulties and increased costs [30, 31]. Hence, other approaches such as immersion lithography, multi-patterning processes and laser interference lithography have been developed to enable the fabrication of smaller features with low costs.

In immersion lithography the conventional air gap between the illumination system and the photoresist is filled with a transparent high refractive index material. Even though this technique increases the numerical aperture and the resolution, it is also quite expensive. Multi-patterning processes suffer from misalignment problems instead [32]. In laser interference lithography the photoresist is illuminated by two light beams with high spatial and temporal coherence, which create a periodic fringe pattern due to constructive and destructive interferences. This low cost technique enables a high resolution, but has reduced flexibility because it is applicable only for defining periodic patterns. Due to this limitation, the laser interference lithography must rely on alternative approaches to create non-periodic features like grating phase shifts [33].

### 3.3 Nanoimprint lithography

There are two main types of NIL; thermal NIL [34] and ultraviolet (UV-)NIL. In thermal and UV-NIL the substrate is coated with a resist that is a thermal- or UV-curable polymer, respectively. After depositing the resist (e.g. by spin coating) the excess solvent is evaporated by heating. In the following steps a mechanical mold (i.e. a stamp) is pressed against the resist, forcing it to conform to the shape of the mold. The resist is cured, having the stamp pressed on it, by increasing the temperature or by irradiating with UV-light. The subsequent stamp separation from the mold is facilitated by anti-adhesion coating of the stamp prior to imprinting. After stamp separation, the residual resist layer from the imprinted/depressed areas is removed. This induces resolution limitations since the removal of the residual layer also removes some of the resist from the un-pressed areas, reducing the remaining resist feature size. Other resolution limitations are related to the viscosity of the resist, to the stamp structure (which, for example, should allow the flow of the resist away from the pressed areas) and to the mechanical stability of the resist structure after imprinting. Half-pitch resolutions from 12.5 nm to 50 nm [35, 36] have been reached with soft stamp UV-NIL. In addition it has been demonstrated that a  $\sim 20$  nm [37] overlay accuracy can be achieved with interferometric Moire patterns.

Both thermal and UV-NIL are relatively inexpensive when compared to EBL in a large scale mass production because relatively large patterns can be replicated by a single imprint and the same stamp can be used to copy the pattern repeatedly on different wafers. Moreover, the stamp can be easily replicated many times from the original master template. The UV-NIL process sequence is illustrated in Figure 3.3.

The NIL step is relatively fast and several wafer-scale imprints can be made in an hour even without automation. Unlike radiation based methods, UV-NIL does not suffer from the diffraction limit in resolution or from substrate backscattering. UV-NIL employs quite basic UV sensitive resists and inexpensive imprint and illumination systems. Typically just a relatively primitive mercury vapor lamp can be used as a light source to replicate high resolution patterns in the nanoscale (sub-100 nm features). Thus, the material and equipment cost are low. UV-NIL is also flexible and many features such as non-periodic structures, phase shifts, grating apodization and chirp can be transferred from the master template without any supplementary process steps.



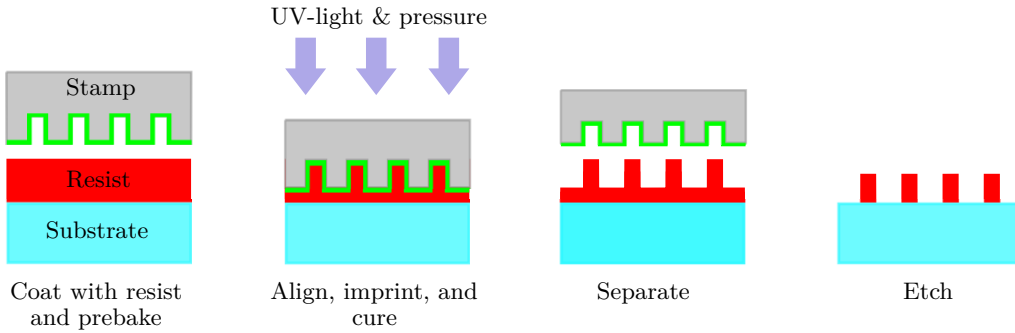


**Figure 3.3:** UV-NIL process illustration. The green layer in the stamp represents the anti-adhesion layer.

UV-NIL has some technological advantages when compared to thermal NIL, particularly in mass production. Due to the thermal cycle, the overlay accuracy of thermal NIL depends on the mismatch of the thermal expansion coefficients of the mold, the resist, and the substrate. Hence, the substrate and the stamp are usually made from the same material but this prevents the use of transparent stamps, which makes the alignment more difficult in thermal NIL [38]. For these reasons the overlay accuracy of thermal NIL is poorer than in UV-NIL. Moreover, the throughput of thermal NIL strongly depends on the used thermoplastic. The process time is usually dominated by the heating, curing, and cooling times of the thermoplastic. With typical thermoplastics these steps can take minutes to carry out. Furthermore, thermoplastics polymer films require a higher imprint pressure than low viscosity UV-NIL monomer resists [38], which increases the cost of thermal NIL imprint systems compared to UV-NIL systems.

As all the other known lithography methods, NIL has also some drawbacks. Because there is a mechanical contact between the stamp and the resist layer in the imprint process, the stamp, the replication pattern, and the substrate are sensitive to defects, surface roughness and non-flatness, residual particles and contamination. For example, a large residual particle, a physical damage in the stamp or a relatively small amount of the resist stuck in the stamp can ruin the following imprints or even break the brittle semiconductor substrate. Multi-layer soft elastomeric stamps have been developed to alleviate the imprint process sensitivity to defects, residual particles, surface roughness and non-flatness [39]. Figure 3.4 shows a soft UV-NIL stamp, which comprises a thick carrier glass, covered by a soft polydimethylsiloxane (PDMS) cushion, a thin layer of glass, a hard PDMS layer and the anti-adhesion layer. The carrier glass gives mechanical rigidity for the stamp and helps the handling and usage of the stamp with some imprint systems. The soft PDMS cushion layer provides the stamp flexibility. The thin glass prevents the lateral deformation of the stamp and the hard PDMS bears the structure to be imprinted. The hard PDMS is coated with a thin layer of Optool anti-adhesion compound to facilitate the stamp separation after imprint.

The softness and flexibility of the stamp leads to more uniform pressure in the imprint area, enabling the stamp to conform to the shapes of defects on the substrate and other non-idealities. Also different anti-adhesion treatments and release agents are used to prevent the contamination of the stamp surface [40]. A layer of anti-adhesion material lowers the surface energy of the stamp, increases the stamp lifetime, device yield, grating quality, and repeatability.

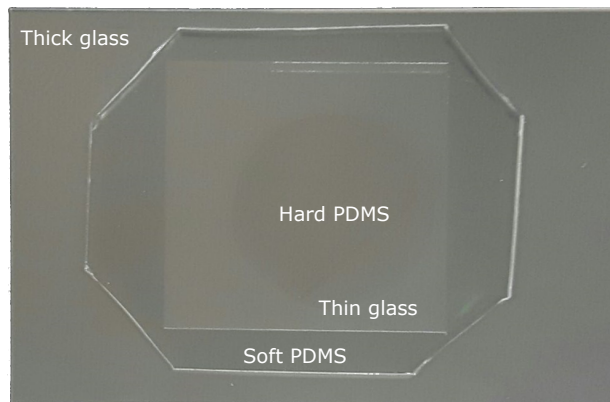


**Figure 3.4:** A soft UV-NIL stamp on a gray opaque background.

Another drawback of NIL comes from the fact that the resolution of the master template and the stamp must be the same as in the imprinted pattern. Therefore a high resolution lithography such as EBL is required to fabricate the master templates.



# 4 Design of narrow-linewidth DFB and DBR lasers

The short and long term spectral stability of the single-frequency laser emission are critical characteristics for many laser applications. The long term spectral stability is related to how accurately a fabricated laser can maintain its emission wavelength and it is affected by external perturbations such as a temperature or bias changes and by internal changes such as degradation or aging. The short term spectral stability of the single-frequency semiconductor laser is related to the temporal coherence of the laser and is given by phase noise. The phase noise is produced by internal sources (e.g. quantum noise), inducing a Lorentzian emission lineshape [41], and by external noise sources (i.e. technical noise), inducing a Gaussian emission lineshape [42, 43]. As a result, the single-frequency semiconductor laser has a Voigt lineshape, generated from the convolution of these Gaussian and Lorentzian lineshapes [43]. The linewidth of the laser emission is the measure of the short term spectral stability.

To design and fabricate single-frequency narrow linewidth semiconductor lasers with low costs is a complicated problem, particularly if lasers must also generate high power levels with good efficiency, reliability and lifetime. In this chapter the problem is investigated from the design point of view for semiconductor edge-emitting DFB and DBR lasers with LC-RWG and ET-RWG surface gratings.

## 4.1 Linewidth theory

In the first theoretical approximation the photons emitted by a lasing laser are monochromatic, directional, and mutually temporally and spatially coherent because the photons are generated by the stimulated emission in a cavity where the light waves are generated according to constructive and destructive interference. However, this picture is idealized and in reality the lasers' emission has a finite spectral width due to several detrimental effects that widen the emission linewidth.

The linewidth of a laser originates fundamentally from spontaneous emission events that inevitably occur in the laser cavity. Spontaneous emission is a process in which photons are emitted temporally and spatially random (i.e. the spontaneous emission events occur at random times and into a random direction). Some of these spontaneously emitted photons are coupled into the lasing mode inducing phase fluctuations in the laser emission, in a manner analogous to the random walk of a classical particle in Brownian motion in space [44]. Consequently, the phase variations of the laser emission follow a Gaussian probability distribution in time domain, resulting in a Lorentzian power spectrum [41, 45].

This gives the fundamental limit for a linewidth for any laser independently of the gain material and of the laser structure.

The broadening caused by spontaneous emission is not the only process and mechanism that broadens the laser linewidth. Flemming and Mooradian [46] were among the first that measured the linewidth of an LD accurately. These measurement showed that the lineshape is Lorentzian, but the linewidth of the measured AlGaAs LD was about 50 times broader than expected according to the prevailing LDs linewidth theory. This prevailing linewidth theory took into account only the broadening caused by spontaneous emission. Henry [9] introduced a linewidth enhancement factor ( $\alpha_H$ ) and proposed that the large deviation from the theory was caused by the coupling of the real and imaginary parts of the refractive index. This factor was predicted to bring a  $(1+\alpha_H^2)$  times broadening to the laser linewidth, leading to the following FWHM linewidth formula for a LD with a Lorentzian lineshape [9]:

$$\Delta\nu = \frac{\pi}{\tau_{coh}} = \frac{R_{sp}}{4\pi F}(1 + \alpha_H^2), \quad (4.1)$$

where  $\Delta\nu$  is the laser linewidth,  $\tau_{coh}$  is the coherence time,  $R_{sp}$  is the time-averaged total spontaneous emission rate coupled to the lasing mode in the laser cavity, and  $F$  is the time averaged total photon number in the laser cavity.

Historically the linewidth enhancement factor was first experimentally determined for a LD using different methods [47–50] and later different theoretical models were developed to predict the factor [51, 52]. The linewidth enhancement factor is defined by:

$$\alpha_H = -\frac{4\pi}{\lambda} \frac{\frac{\partial n}{\partial N}}{\frac{\partial g}{\partial N}}, \quad (4.2)$$

where  $\lambda$  is the emission wavelength,  $g$  is the material gain,  $n$  is the refractive index and  $N$  is the carrier density.

Assuming an exponentially increasing photon density in the laser cavity, Equation (4.1) can be expressed as [9, 53]:

$$\Delta\nu = \frac{v_g^2 h \nu n_{sp} \alpha_m (\alpha_m + \alpha_i)}{8\pi P_0} (1 + \alpha_H^2) K_c, \quad (4.3)$$

for a single mode Fabry-Perot laser. In Equation (4.3)  $v_g$  is the group velocity,  $h$  is the Planck constant,  $\nu$  is optical frequency,  $n_{sp}$  is the population inversion factor,  $\alpha_m$  is the mirror loss factor per unit length,  $\alpha_i$  is the internal loss factor per unit length, and  $K_c$  is the Petermann factor. The population inversion factor is given by:

$$n_{sp} = \frac{1}{1 - \exp[-(qV - h\nu)/kT]}, \quad (4.4)$$

where  $q$  is the elementary charge,  $V$  is the potential difference between quasi-Fermi levels,  $h$  is the Planck constant and  $\nu$  is the optical frequency.

The Petermann factor can be written as [54, 55]:

$$K_c = \left| \frac{\int \int \int |\Psi(x, y, z)|^2 dV}{\int \int \int \Psi^2(x, y, z) dV} \right|^2, \quad (4.5)$$

where  $\Psi$  is the optical field amplitude in the laser cavity. The output power per facet ( $P_0$ ) above the threshold current ( $I_{th}$ ) is given by [53]:

$$P_0 = \frac{h\nu\eta_i(I - I_{th})}{q} \frac{\alpha_m}{\alpha_m + \alpha_i}, \quad \text{with } I_{th} = \frac{qV_{act}N_{th}}{\tau_c}, \quad (4.6)$$

where  $q$  is the elementary charge,  $\eta_i$  is the internal quantum efficiency,  $I$  is the bias current,  $V_{act}$  is the active region volume,  $N_{th}$  threshold carrier density, and  $\tau_c$  is the carrier lifetime.

According to Equations (4.3) and (4.6) there are several factors that can be influenced by the design in order to narrow the emission linewidth:

- Lower internal loss results in a sizable reduction in the laser linewidth. Moreover, a decrease in the internal losses leads to a smaller threshold current and increased slope efficiency. Lower internal losses can be obtained by minimizing the defect density in the active and guiding regions, and optimizing the doping profile (e.g. decreasing free carrier absorption through a doping profile that overlaps as little as possible with the optical field distribution)
- A reduction in the mirror losses narrows the linewidth. Moreover, smaller mirror losses reduce the threshold current (i.e. smaller mirror losses decrease the threshold carrier density) but also decrease the slope efficiency, reducing the maximum achievable output power.
- A smaller linewidth enhancement factor reduces the linewidth. The linewidth enhancement can be reduced by increasing the differential gain through blue-shifting the grating resonance with respect to the gain peak [56]
- The Petermann factor describes the enhancement of quantum noise [57]. For an index guided optical mode the Petermann factor is close to unity, but for gain guided modes the  $K_c$  factor is higher [58].
- A higher injection efficiency decreases the linewidth and increases the output power. High injection efficiency can be achieved by minimizing the current leakages.
- Smaller  $V_{act}$  reduces the threshold current which leads to higher power, better wall-plug efficiency, and smaller emission linewidth. Therefore single QW structures are preferred, particularly if the total loss level is low enough so that the gain saturation is not reached.
- The threshold current and the linewidth can be reduced by increasing the carrier lifetime. A lower defect density and a lower Auger recombination rate increase the carrier lifetime. The Auger recombinations are reduced by strained active regions and energy level engineering.

As Equations (4.3) and (4.6) indicate, the linewidth theory of LDs predicts that the linewidth should monotonically narrow for a single mode LD as the bias current and output power increase. However, the measured linewidth variations with bias and power for a typical DFB laser indicate that the linewidth can also increase with increasing bias current after it has reached a certain linewidth floor [59, 60]. A similar behavior has also been observed in DBR lasers [61]. This linewidth re-broadening of LDs, which is

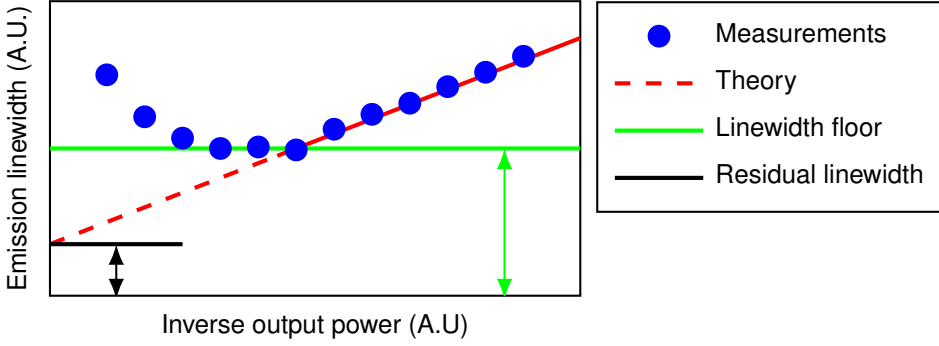


**Figure 4.1:** The sketch shows the typical behavior of the linewidth for a DFB laser as a function of inverse output power per facet.

not explained by the general linewidth theory [9, 41, 62], limits the narrowest attainable intrinsic linewidth and the single mode operation regime of a LD [63].

Figure 4.1 illustrates the typical linewidth power dependency of a DFB laser. It indicates that after a certain power level the laser linewidth narrowing saturates and the linewidth starts to broaden as the device is pumped harder and the output power increases. This is in contradiction with the general linewidth theory. The saturated/effective minimum linewidth is called the linewidth floor, whereas the residual linewidth is the theoretical minimum laser linewidth for an infinite power level. The origin of the residual linewidth is derived from  $1/f$  noise [64, 65].

The linewidth re-broadening has been explained by various effects such as lateral spatial hole burning (SHB) [66], longitudinal SHB [67], the presence of side modes [68], gain compression and spectral hole burning [69], mode instability [70], and spontaneous emission noise in the separate confinement heterostructure (SCH)/barrier layers [71]. Hence, in order to fabricate a narrow linewidth LD, various phenomena must be taken into account and, therefore, numeric and/or analytic simulations and experimental investigations are required to find the optimal device parameters for narrow linewidth emission. These experimental, analytic and numeric optimizations are discussed more thoroughly later in this thesis. A detailed discussion of the device parameters in Equations (4.3) and (4.6) and on their influence on linewidth can also be found in [Pub1].

#### 4.1.1 External linewidth broadening

There are also other noise sources that contribute to the measured spectral width of a laser line besides the internal sources discussed in Section 4.1. These noise sources have a technical origin and the associated noise is called technical noise.

For example fluctuations in the injection current density can lead to carrier and photon density variations in the device cavity, which can in turn induce temporal variations of the temperature distribution in the device. In addition to un-stabilized temperature, these fluctuations can induce a change in the material gain and in the effective refractive index, broadening the spectral width of a LD [72]. Mechanical vibrations and variations in the ambient pressure may broaden the linewidth of LDs slightly, but these noise sources are

usually a problem only for external cavity lasers, not for mechanically robust monolithic DFB and DBR lasers.

External noise sources (i.e. thermal noise and bias current variations) have typically a Gaussian frequency spectrum and the laser lineshape results as a Voigt function from the convolution of the internal/intrinsic Lorentzian lineshape and the technical noise lineshape. The intrinsic Lorentzian linewidth can be extracted from the convoluted Voigt lineshape, enabling to evaluate how much of the linewidth originates from the laser internal noise.

## 4.2 DFB and DBR lasers

DFB and DBR lasers have a very essential structural difference. The DFB lasers have a feedback grating structure integrated with the gain section, whereas the DBR lasers have separate grating and gain sections. This key structural difference introduces other differences in the design, fabrication, operation, and characteristics of these devices.

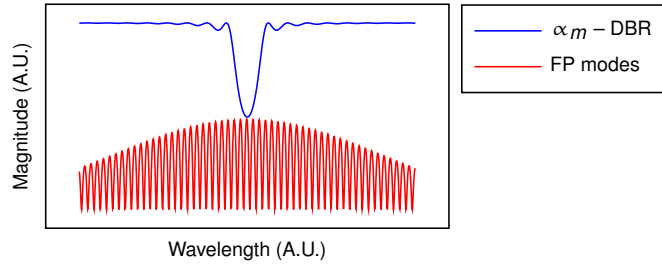


**Figure 4.2:** Sketch depicting the longitudinal mode selection of a DBR laser with one distributed Bragg reflector end mirror ( $\kappa \cdot L = 1$ ). The convolution between the gain envelope and the FP modes (red) combined with the mirror loss of the DBR mirror (blue) determines the lasing longitudinal mode.

Ideally a DBR laser acts as a FP laser with at least one distributed Bragg reflector end mirror, which has a relatively narrow stopband width when compared to the gain bandwidth. A convolution between the FP modes and the DBR mirror reflectivity selects the longitudinal modes supported by the cavity. The overlap between the gain and the supported modes determines which of the longitudinal modes reaches the threshold first, starts lasing, and dominates the gain competition between the longitudinal modes. Multiple grating sections can also be used to filter longitudinal modes. Even though these devices can reach narrower linewidths [73], the fabrication of multi-section DBR lasers with multiple contacts is complicated.

A DFB laser with a uniform grating structure has a transmission spectrum where a stopband (i.e. a spectral region where no longitudinal modes satisfy the phase condition) and side lobes on both sides of the stopband appear. An index-coupled DFB laser (i.e. having mainly real part effective refractive index longitudinal variation in the grating) with a uniform grating, symmetric facet reflectivities and the gain spectrum centered on the stopband emits two degenerate longitudinal modes at the transmission maxima placed next to the short and long wavelength limits of the stopband. Asymmetries must be introduced to the DFB laser structure in order to remove the emission mode degeneracy and obtain single longitudinal mode operation. These asymmetries might be deliberately



introduced or might simply result from fabrication imperfections or from the alignment of the gain spectrum with the stopband.

When asymmetries are not deliberately introduced, depending on the end facet reflections (i.e. phases and magnitudes), loss/gain coupling, imperfections in the device fabrication, and the relative spectral position of the gain peak and stopband, one of the longitudinal modes at the side lobe transmission maxima next to the stopband is first to get enough gain to overcome the mirror and internal losses and starts to lase. Typically the mode that starts to lase first is located either on the blue or the red edge of the stopband.

However, due to the fabrication imperfections and inaccuracy, it is not clear which one of the modes starts to lase first in a DFB laser with a uniform purely index coupled grating structure because the mirror loss difference between these modes vanishes in this case (see Figure 4.3). Hence, the mode selection based on un-intentionally introduced asymmetries is not controllable and reproducible across a device batch. Even when deliberately introducing some asymmetry (like anti-reflection and high-reflection facet coatings) the longitudinal mode selection remains tricky and not fully reproducible.

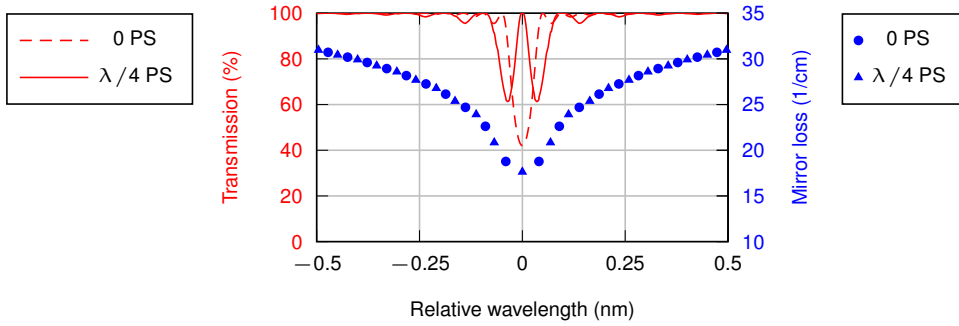


**Figure 4.3:** The mirror losses (dots and triangles) and the grating transmission (dashed and continuous line) calculated using coupled mode theory for a DFB laser without a PS and for a DFB laser with a  $\lambda/4$  PS. The  $\kappa \cdot L$ -product is 1 in both cases and the end facet reflections are neglected.

A more reproducible way to eliminate mode degeneracy and induce stable single longitudinal mode operation is to introduce a defect mode in the stopband. The introduction of a defect mode in the stopband, for example by placing a quarter wavelength long PS in the cavity, creates a microcavity structure that favors a longitudinal mode at the grating Bragg resonance. This favored mode is likely to start to lase first and dominate the mode competition if the spectral position of the gain peak is aligned properly with respect to the Bragg resonance wavelength.

DFB and DBR lasers have different wavelength tuning and mode-hop mechanisms. In DFB lasers a bias current or temperature increase red-shifts the Bragg resonance and the emission wavelength mainly due to temperature-induced refractive index change. The temperature increase also red-shifts the gain spectrum. Because the temperature-induced red-shift of the gain is bigger than the red-shift of the Bragg resonance, at some point another mode becomes better aligned with the gain peak, resulting in a mode jump and an abrupt emission wavelength change, usually associated with the termination of single-longitudinal mode DFB operation. However, since the stopband is generally large

and the Bragg resonance and gain spectrum are both red-shifting, the wavelength tuning in single-mode DFB operation (i.e. the mode-hop-free tuning range) is rather large.

Because DBR lasers have separate gain and feedback sections the gratings are usually passive/lossy sections (or transparent sections when they have their own contact). This means that the change in the gain section injection current does not ideally (i.e. without thermal or carrier leakage) affect the envelope of the grating reflectivity. Thus, the mode-hop-free tuning range of the emission wavelength is limited by the free spectral range of the device cavity, which is usually much shorter than the mode-hop-free tuning range of the DFB lasers. Although more closely spaced, the mode hops in DBR lasers are more predictable as the wavelength tuning retraces a similar range between mode hops and the mode hops do not terminate the single-mode operation. In order to widen the mode-hop-free tuning range of DBR lasers, advanced grating structures and multi-section DBR lasers have been introduced [53], but the fabrication of these complex structures is complicated.

Since the grating structure in DBR lasers is passive, the grating length is preferably short for lasers targeting at narrow linewidth because the passive section does not have a population inversion and thus an incoming photon can be absorbed. Since the photon density decays in the grating section, due to absorption and grating reflectivity, it is likely that the absorbed photons are later emitted through spontaneous emission instead of stimulated emission. This broadens the emission linewidth. The linewidth broadening by spontaneous emission is reduced when the grating is short and the photon density decay in the grating is dominated by reflection and not by absorption (i.e. when the grating coupling coefficient is high). A short grating length must also be associated with a high coupling coefficient in order to ensure the mode selection with a high side mode suppression ratio (SMSR). On the other hand a high coupling coefficient is known to lead to longitudinal SHB which eventually promotes side modes and linewidth re-broadening effects. Thus, it is relatively difficult to obtain very narrow linewidth emission from DBR lasers. As an advantage, the output power of the DBR lasers can be scaled up relatively easy, by increasing the volume and the bias applied to the gain section, particularly when only one DBR mirror is employed at the back end of the cavity and anti-reflection coating is used on the front end facet.

The most effective and straightforward way for reducing the linewidth of DFB lasers, according to Equation (4.3), is by decreasing the mirror losses. The mirror losses are reduced by a high coupling strength ( $\kappa \cdot L$ ), which also decreases the slope efficiency (see Equation (4.6)). Consequently, while reducing the emission linewidth, a high coupling strength can limit the saturated output power level. Also a high coupling coefficient improves the SMSR but induces rapid longitudinal variations in the photon density favoring SHB. A long DFB grating with a low coupling coefficient, having a good coupling strength and relatively flat longitudinal photon and carrier distributions has the best chances to emit a stable single mode with a very narrow linewidth. Unfortunately, such a structure can only generate a limited output power because of the small output coupling resulted from the low mirror losses. Hence, it is critical to optimize the grating structure for both DFB and DBR lasers in order to reach both a narrow emission linewidth and a good output power [Pub1].



higher order transverse modes have a higher coupling coefficient and, consequently, lower mirror losses),

- low internal losses (i.e. minimized free-carrier absorption, small scattering losses, low defect density),
- small potential barriers along the path of carrier injection and a low series resistance,
- a large near-field spot size to improve the device reliability by lowering the power density on the output facet as well as to reduce the FWHM width of the far-field intensity pattern,
- low thermal resistance that enables a high saturation power level.

Most of these requirements are contradictory coupled (i.e. when one is improved, the other is worsened) through their dependencies on the laser structural parameters:

- the transverse confinement factor in the gain region is contradictory coupled both with the transverse confinement factor in the surface grating regions and with the near-field spot size,
- the modal gain discrimination is contradictory coupled with the series resistance for certain ranges of the central ridge width and lateral extension of the gratings,
- the free carrier absorption is contradictory coupled with the confinement factor in the grating regions and with the near field spot size through the overlapping of the doping profile with the transverse optical field distribution,
- the transverse carrier confinement is contradictory coupled with the coupling coefficient for certain ranges of the lateral extension of the gratings,
- the series resistance and the coupling coefficient are contradictory coupled through the width of the central ridge,
- the free carrier absorption and the coupling coefficient are contradictory coupled through the doping profile and cladding layer thickness.

The QWs, whose thickness is in the order of the de Broglie wavelength (i.e. typically a few nanometers), possess smaller  $n_{sp}$  and  $(1 + \alpha_H^2)$  factors at low total loss levels [74], better temperature stability [75], higher internal efficiency [53] and lower threshold current densities [76]. Also the QW structures can employ strain, which enables easier population inversion (by removing the heavy-hole light-hole energy level degeneracy) and reduction in the Auger recombination [77].

The choice of quantum well number depends on the loss level. Single QW active regions have smaller active region volume, leading to a smaller transparency carrier density than multi-QW structures because only the states of the single QW must be inverted. However, at high loss levels multi-QW active region structures can achieve a smaller  $n_{sp} * (1 + \alpha_H^2)$ -factor [74] and a lower transparency carrier density compared to single QW structures due to the gain saturation of single QW active regions at high injection levels [78]. Because the emission linewidth is proportional to  $(\alpha_i + \alpha_m)^2$ , according to Equations (4.3) and (4.6), the narrow linewidth lasers are designed to have relatively low loss levels. Consequently, single QW laser structures are generally seen as the best choice

for narrow linewidth LDs as long as low losses can be achieved. Moreover, multi-QW active regions are also more difficult to design and grow because the different carrier transport effects and the coupling between neighboring wells must be taken into account.

From the design point of view the thickness of the QW and the compositions of the QW and the waveguides should be optimized to achieve the target emission wavelength, good carrier capture into and low carrier escape from the well. Moreover, strained wells can decrease the linewidth enhancement factor [79] and improve discrimination between transverse magnetic (TM) and transverse electric (TE) modes [77]. Both of these effects are expected to decrease the emission linewidth. Particularly compressive strain is beneficial in the QW because in this case both the gratings and the quantum well strain favor more TE than TM modes.

When designing the epilayer structure for LDs with surface gratings, the waveguide layers' thickness and refractive index contrast with respect to the cladding layers are optimized to achieve a good QW optical confinement but also to achieve sufficient penetration of the optical field tails into the cladding region. The optical field tail in the top cladding provides good coupling of the surface gratings with the optical field, ensuring the required optical feedback for the optical field propagating in the longitudinal direction of the cavity. The waveguide layers are also made wide enough to accommodate a large area fundamental TE mode. This enables a high output power without excessive near optical field power densities, which lessens the probability of catastrophic optical damage of the facets. A stable single transverse mode operation is obtained by designing the etch depth and the ridge width sufficiently deep and wide to provide higher modal gain for the fundamental mode and less modal gain and/or increased losses for the higher order and TM modes [80].

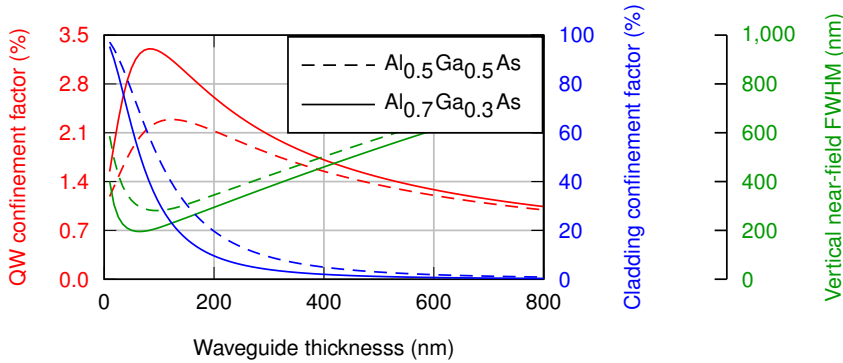


**Figure 4.5:** QW and cladding layers' optical confinement factor variation with  $\text{Al}_{0.35}\text{Ga}_{0.65}\text{As}$  waveguide layers' thickness in a 780 nm LD for two cladding layer compositions ( $\text{Al}_{0.50}\text{Ga}_{0.50}\text{As}$  and  $\text{Al}_{0.70}\text{Ga}_{0.30}\text{As}$ ). The figure illustrates that a higher refractive index contrast between the cladding and the waveguide is beneficial in terms of the optical QW confinement factor but reduces the optical field tails into the cladding layers, decreasing the achievable surface grating coupling coefficient and the near-field spot size.

The composition and the thickness of the cladding layers are optimized to confine the carriers in the waveguide layers, prevent the optical field from penetrating into the substrate and into the highly doped contact layer and to provide optical contrast to the waveguide layers in order to achieve good optical confinement in the QW. The cladding

thickness must achieve a good compromise between providing optical field tails close enough to the epilayer surface (for achieving sufficient grating coupling coefficient without deep etching of the surface gratings) and avoiding the coupling of the optical field with the highly doped top contact layer. The cladding layers must have high doping levels to ensure good carrier injection and low series resistance but, on the other hand, they still should have low doping in the areas with optical field tails, in order to reduce free carrier absorption. A doping profile that reverse-mirrors the optical field profile in the claddings (i.e. high doping where the optical field intensity is low and low doping where the optical field intensity is high) provides a good doping compromise.

Barrier reduction layers are sometimes introduced between the cladding and substrate layers and/or between the cladding and contact layers when the substrate and/or the contact layers have much smaller bandgaps than the cladding layers. These barrier reduction layers ease the carrier flow from the highly p-doped contact layers to the p-type cladding layer and from the n-type substrate to the n-type cladding layer. Moreover, the doping profiles are optimized to reduce or eliminate energy level notches at the heterointerfaces.

Because surface gratings are employed, the epilayer structure does not require special grating layers. However, in order to accurately control the etching depth and minimize etching depth variations, a thin etch-stop layer of a material that has significantly different etch properties can be included. It should be noted that a high bandgap etch-stop layer can also create a barrier for carriers, hampering the carrier flow into the active region. It is also possible that the compositional variation between the top p-side cladding and waveguide layers creates an etch-stop at their interface (like in the case of GaInP waveguide layers embedded in AlGaAs cladding layers).

## 4.4 Longitudinal structure

According to Equations (4.3) and (4.6), the emission linewidth narrows as the internal and mirror losses decrease. The DFB laser linewidth narrowing with increasing coupling strength (i.e.  $\kappa \cdot L$ -product), which implies reducing the mirror loss, is shown in the left panel of Figure 4.6. The left panel also shows that at short cavity lengths the coupling coefficient has a large effect on the emission linewidth, while at long cavities the effect of coupling coefficient on the emission linewidth is much smaller. Furthermore, a reduction in the mirror losses leads to a decrease in the threshold current but also to a decrease in the slope efficiency, limiting the maximum achievable output power. Therefore, there is an optimum device length that maximizes the output power for a given injection current density and a given coupling coefficient. This is depicted in the right panel of Figure 4.6, which shows that the maximum achievable output power increases when the grating coupling coefficient is reduced.

The analytic Equations (4.3) and (4.6) do not take into account some important effects such as longitudinal SHB and the presence of side modes. The longitudinal photon and carrier densities in DFB and DBR LDs are not uniform along the length of the device due to various effects and non-idealities. Particularly, multi-section devices can have very significant variations in the longitudinal photon and carrier densities. The non-uniform longitudinal photon density, carrier density and gain/loss distributions can affect the device performance in many different ways and induce phenomena that are detrimental for the emission linewidth, output power, and device lifetime. Hence, it is vital to investigate and analyze the longitudinal non-uniformities in DFB and DBR

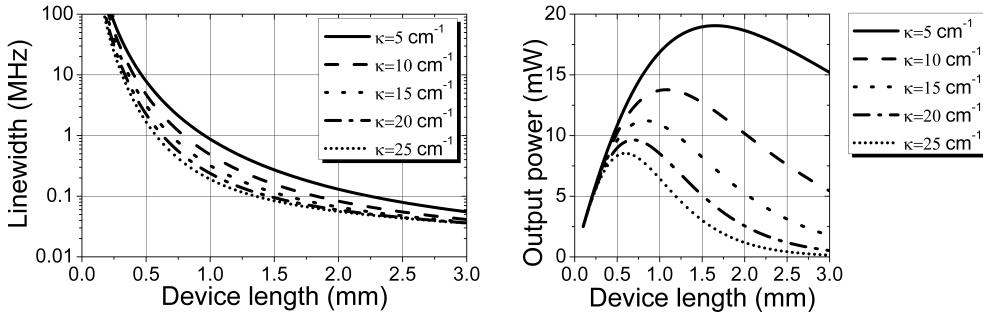


**Figure 4.6:** The emission linewidth (left panel) and the output power per facet (right panel) calculated using Equations (4.3) and (4.6) for a 780 nm DFB laser with varying cavity length and grating coupling coefficient. The end facet reflectivities are 1% and 90%. [Pub1] reproduced with permission.

lasers. A time domain traveling wave (TDTW) model has been developed to investigate the longitudinal non-uniformities of the carrier and photon densities and to give a more realistic approximation of the device characteristics [Pub1]. The model has been used to analyze the longitudinal carrier and photon densities of DFB lasers with 0 PS and anti-reflection (AR)/high-reflection (HR)-coated facets, with  $1 \times \lambda/4$  PS and AR-coated facets, and with  $2 \times \lambda/8$  PS and AR-coated facets since these device structures are typically used to remove the degeneracy of longitudinal modes in DFB cavities. The simulation results calculated according to this model predict that the SMSR of the DFB lasers degrades as the cavity reaches a certain length at a given injection current density and coupling coefficient, which is shown in Figure 4.7.

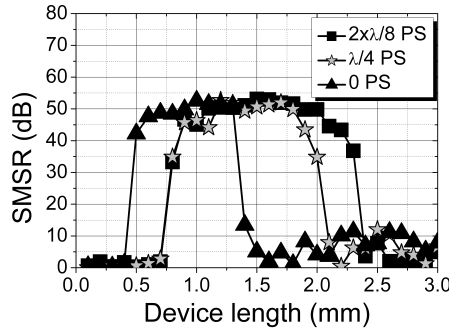


**Figure 4.7:** SMSR as a function of laser length for DFB lasers with different phase shift configurations. The DFB without phase shifts has facet reflectivities of 1%/90% and the phase shifted DFB lasers have 1%/1% facet reflectivities. The facets of each device variant are phase matched with the gratings. In each of the TDTW calculations a grating coupling coefficient of  $7.5 \text{ cm}^{-1}$  and an injection current density of  $6.25 \text{ kA cm}^{-2}$  have been used. [Pub1] reproduced with permission.

Figure 4.7 indicates that the DFB laser with no phase shift and 1%/90% facet reflectivities has the most limited single mode operation regime of all three simulated DFB laser structures. Figure 4.7 also shows that the DFB laser with  $2 \times \lambda/8$  phase-shifts and 1%/1%

end facet reflectivities allows the longest cavity to operate in a single longitudinal mode. From the design point of view this observation has a notable impact. If the device cavity is short, the AR/HR-coated DFB laser with no phase shifts has the narrowest linewidth and the highest power at a given injection current density and coupling coefficient (as shown in Figure 4.8). Because the AR-coated phase shifted DFB lasers allow single longitudinal mode operation for longer cavities with a given coupling coefficient and injection current density, these long cavity lasers can still provide a narrower linewidth with similar power levels when compared with the AR/HR-coated DFB laser with no phase shifts as shown in Figure 4.8. On the other hand longer cavity lengths with the same injection current density and similar power levels mean that the wall-plug efficiency is usually smaller for these long cavity AR-coated phase shifted DFB lasers than for short cavity AR/HR-coated DFB lasers without a phase shift.

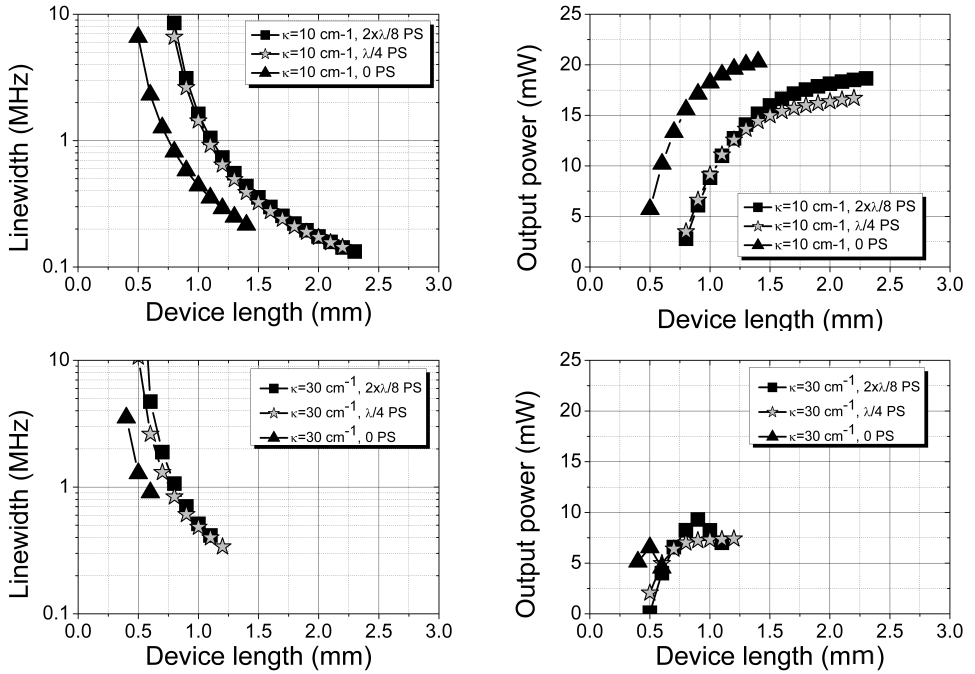


**Figure 4.8:** Spectral linewidths and output powers for DFB lasers with different phase shift configurations and coupling coefficient of either 10 or  $30 \text{ cm}^{-1}$ . The facet reflectivities of the devices with zero phase shifts were 1%/99% and the other device variants had 1%/1% facet reflectivity values. All facet reflectivities were phase-matched to the gratings. The shown points correspond to the operation range where the devices emitted in single longitudinal mode with higher than 35 dB SMSR. [Pub1] reproduced with permission.

It should be however noted that the characteristics of the AR/HR-coated DFB lasers have a strong dependency on the phase matching between the HR-coated facet and the gratings, while the characteristics of the AR/AR-coated DFB lasers have a negligible dependency on the phase matching between the AR-coated facets and the gratings. Since the facet phase matching with the gratings is random (due to the fact that typically the cleaved facet positions cannot be controlled accurately enough with respect to the grating), this means that the results obtained with phase-matched AR/HR-coated facets



are obtained for the best case of facet position, which seldom occurs in reality.

As a general conclusion, the simulation results shown in Figure 4.8 point out that the combination of a long cavity with a low coupling coefficient and AR/AR-coated facets should provide the narrowest linewidth at the highest possible power with an elevated yield.

The limited range of single mode operation regime is a consequence of longitudinal SHB. The stimulated emission effectively depletes the carrier density around the anti-nodes of the longitudinal optical field, where the photon density is high. This saturates the optical gain of the lasing dominating longitudinal mode and gives rise to side modes because the antinodes of these modes are not at the same positions as the antinodes of the dominating mode and the gain of these modes is not similarly depleted. Because of this effect, known as longitudinal spatial SHB, it is important to minimize the non-uniformities of the photon and carrier longitudinal distributions in the laser cavity when the laser structure aims for high power narrow linewidth emission.

Figure 4.9 illustrates typical longitudinal photon and carrier density envelopes in DFB lasers for different coupling coefficient values. Figure 4.9 shows that if the coupling coefficient is high, the longitudinal carrier and photon densities can be highly non-uniform.

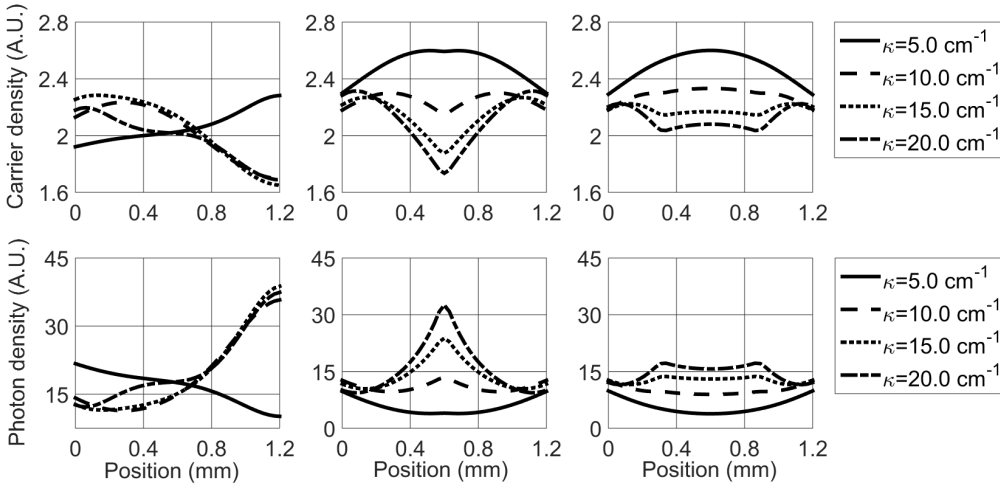


**Figure 4.9:** Longitudinal relative carrier and photon density envelopes as a function of cavity position in DFB lasers with different phase shift configurations. The devices without phase shifts have 1%/90% facet reflectivities, whereas the ones with phase shifts have 1%/1% facet reflectivities. All the facets are phase matched with the gratings. The injection current density was 6.25 kA/cm<sup>2</sup> and the other model parameters used in the TDTW are in Table 8.1. [Pub1] reproduced with permission.

The coupling coefficient has many effects on the device operation and characteristics. For example, in the AR/HR-coated DFB laser with no phase shift the photon density at the AR-coated output facet (positioned at 0 mm in the cavity) decreases with increasing coupling coefficient. Once the reflectivity of the grating reaches the reflectivity of the HR-coated end facet, the asymmetry of the longitudinal carrier and photon densities changes rapidly to the opposite side of the cavity. This is shown in the left panels of Figure 4.9. A high photon density builds up into the HR end of the cavity, because

the photons at this end are effectively surrounded by two high reflectivity mirrors that prevent them from escaping the cavity and in the same time the stimulated emission creates new photons that are also trapped in this part of the cavity. The presence of phase-shifts reduces and symmetrizes the longitudinal variations of photon and carrier densities, particularly when the coupling strength is not too high. A longer continuous phase shift region can also be used to reduce spatial hole-burning induced broadening but this also reduces the SMSR and the stability of single mode operation. Figure 4.9 indicates that the DFB laser structure with  $2 \times \lambda/8$  phase-shifts, AR-coated facets and grating strengths around  $\kappa \cdot L=1$  leads to the flattest carrier and photon density distributions.

As Equations (4.3) and (4.6) indicate, low total losses lead to narrow linewidth. In DBR lasers low total losses can be obtained with low internal losses and high reflectivity end mirrors, which require a relatively strong coupling strength ( $\kappa \cdot L$ -product). Moreover, a high coupling strength decreases the coupling of amplified spontaneous emission (ASE) noise to the emission mode. However, a strong coupling strength promotes non-uniform longitudinal carrier and photon density distributions, introducing longitudinal SHB.

Literature reports have pointed out that the output power and emission linewidth of DBR and DFB lasers depend strongly on the termination of the Bragg grating at the rear facet [81]. A high reflectivity rear-end DBR mirror of a DBR laser or the HR-coating of the rear facet of a DFB laser improves the output power but also increases the emission linewidth. This is consistent with our experimental results, which show that DBR lasers have higher output powers but also broader emission linewidths than DFB lasers. It has also been experimentally demonstrated that for DBR lasers with one distributed Bragg reflector end mirror a certain coupling coefficient value minimizes the linewidth for a given grating length and relative current ratio at single mode operation regime  $(I-I_{th})/I_{th}$  [82]. Hence, the DBR lasers require a careful optimization to achieve a narrow emission linewidth, while generally targeting higher output powers but broader emission linewidths as compared with the DFB lasers.

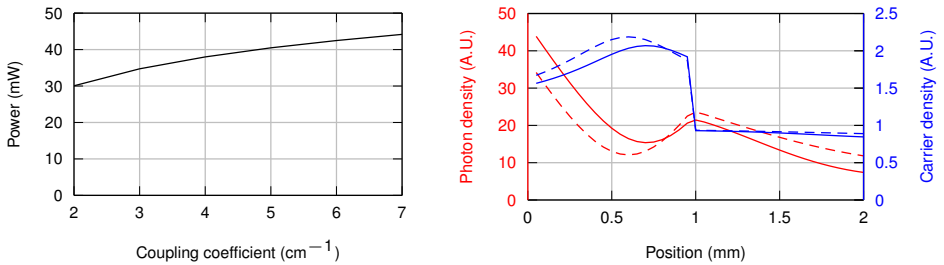


**Figure 4.10:** The left panel shows the output power variation with the coupling coefficient for a DBR laser with a 1 mm long RWG gain section, a 1 mm long unbiased DBR section and phase-matched 3% facet reflectivities. The right panel shows the relative longitudinal photon and carrier density distributions in the cavity of the same laser for the coupling coefficients of  $3 \text{ cm}^{-1}$  (dashed lines) and  $7 \text{ cm}^{-1}$  (solid lines). The RWG section lies between 0 and 1 mm and the DBR section is located between 1 and 2 mm. The results are plotted only in the simulated single mode regime in which the SMSR is above 30 dB. The calculations are made using the TDTW method described in [Pub1]. The modeling parameters are given in Table 8.1 and the carrier density is normalized with respect to the transparency carrier density.

The left panel of Figure 4.10 shows the output power as a variation of the coupling coefficient for a DBR laser with a 1 mm long RWG gain section and a single 1 mm long distributed Bragg reflector end mirror. The panel illustrates that the output power increases monotonically as the coupling coefficient increases for constant RWG and DBR section lengths. The right panel of Figure 4.10 indicates that the higher coupling coefficient induces a more asymmetric photon density distribution with a higher variation due to the better optical feedback. The higher variation and asymmetry depletes the carrier density distribution from the high photon density areas in the RWG section (from 0 mm to 1 mm) and therefore the output power saturates as the coupling coefficient increases. As shown in the right panel of Figure 4.10, a lower coupling coefficient enables a higher photon density in the unbiased DBR grating section (from 1 mm to 2 mm), which is lossy since the carrier density is below the transparency value ( $N < 1$ ). A higher photon density in the DBR section implies increased photon absorption and increased spontaneous re-emission, which broadens the linewidth.

## 4.5 Master oscillator power amplifier laser structure

A multi-section MOPA laser structure can be used to decouple the narrow linewidth and high power requirements and to enable independent control of the emission wavelength and output power. While the MO section should provide a narrow linewidth injection into the SOA PA section, several conditions must be satisfied so that the amplification does not degrade the injected linewidth. An important condition when the MO is a DFB laser is to prevent/limit the reverse optical injection from the SOA section into the MO section. Only an extremely good anti-reflection coating of the SOA facet could reduce the backward reflection into the MO section to the degree required by maintaining a narrow linewidth with SOA amplification. A better solution would be to use tilted facets at both ends (which eliminates also the influence of the uncontrollable phase of the reflection from the facet of the DFB section). The tilted placement of a MOPA design with a DFB MO section and a flared SOA section is illustrated in the sketch given in the left panel of Figure 4.11.

The left panel of Figure 4.11 also shows a pre-amplifier segment at the end of the DFB MO section, before the flared SOA PA section. Without the pre-amplifier segment the input power of the PA section is low due to the low output power of the MO section and to the short unbiased absorbing gap/electrical isolation between the MO and PA sections. The electrical isolation is needed to prevent the current leakage from one section to another because of the different drive voltages resulting mainly from different injection current densities and contact areas. The pre-amplifier segment enhances the output power of the MO section, ensuring a relatively high input power of the PA section. If the output power of the MOPA laser is not limited by the catastrophic optical damage, the enhanced input power of the PA section can enable a shorter PA section with a less wide emitting facet to reach the same saturated power level with the same injection current due to the improved heat dissipation.

When the MO section is a DBR laser (having separate gain and grating sections) the power injected in the SOA section can be increased by stronger pumping of the RWG gain section (but mode hopping problems may arise). For the MOPA with DBR MO the reflection into the MO section is necessary but, since this reflection can be weak, it could be provided by mode mismatching at the MO-PA interface. The right panel of Figure 4.11 shows a sketch of a tilted MOPA design with DBR MO section. The

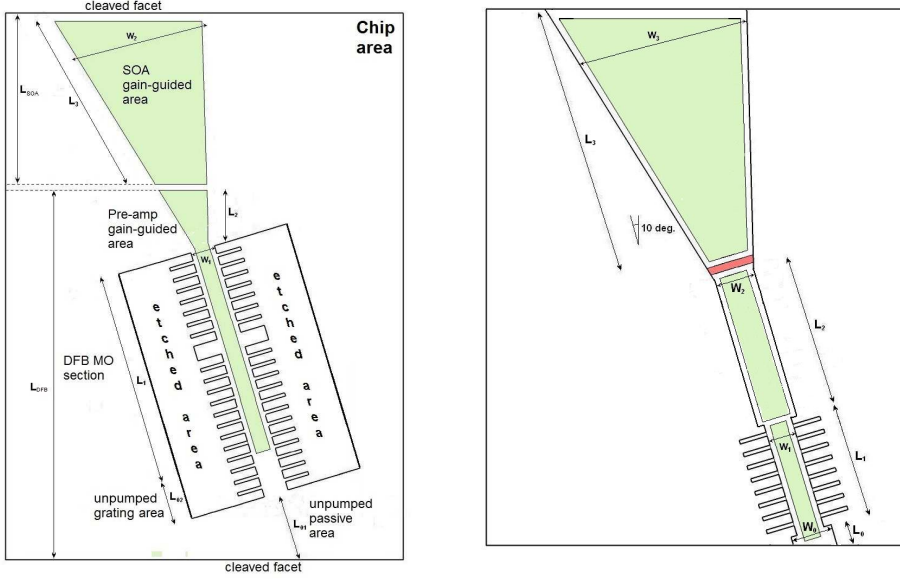


**Figure 4.11:** Top-view sketch of a tilted MOPA with DFB MO section (employing a phase-shift and a pre-amp section) and a flared SOA section (left panel) and top-view sketch of a tilted MOPA with DBR MO section implemented using LC-RWG gratings (right panel). The sketches are not to scale.

DBR part of the MO section can be implemented with etched through ridge gratings (which can achieve higher coupling coefficients) or with LC-RWG gratings, like in the figure (which can achieve lower coupling coefficients). It should be noted that, for a low grating coupling coefficient, the relatively long DBR grating section required for achieving adequate single longitudinal mode selection might require separate biasing (non-passive DBR grating). This is because the monolithic integration leads to high absorption (and increased probability of spontaneous re-emission coupled into the lasing mode) in the DBR grating section when QW intermixing is not employed in the DBR grating section for the reduction of losses (the QW intermixing is avoided in order to keep the fabrication complexity at a minimum). However, the use of three separate contacts (for the DBR grating section, for the RWG gain section and for the flared SOA section) has the advantage that the output power and the emission wavelength can be adjusted/tuned more flexibly (including the possibility of independent locking loops).



# 5 The fabrication of DFB and DBR lasers with surface gratings using soft stamp UV-nanoimprint lithography

In this Chapter the fabrication of DFB and DBR lasers is discussed. The process flow in the fabrication of DFB lasers with LC-RWG surface grating is presented and the main process steps are discussed. Moreover, the differences between the device fabrication of DFB and DBR lasers with surface gratings are discussed and the fabrication limitations of these two different kind of LDs are analyzed in this Chapter. The fabrication flows are discussed briefly in [Pub2], [Pub3], and [Pub4].

## 5.1 Epitaxial growth

The III-V semiconductor epilayer structures used in the studies described in the thesis have been grown with all solid-source molecular beam epitaxy (MBE). The solid-source MBE reactor encloses different elemental group III sources such as aluminum (Al), gallium (Ga), and indium (In) and group V materials such as arsenide ( $\text{As}_4$ ) and phosphorus ( $\text{P}_4$ ) that are cracked to smaller  $\text{As}_2$  and  $\text{P}_2$  molecules before being emitted onto a substrate wafer. The growths have typically been performed on (001) n-GaAs substrates that have a diameter of 2 inch.

The growth parameters have been optimized by growing separate calibration samples before the growth of the final laser structures. Typically, the composition of the quantum well (QW) is calibrated with superlattice samples, and the emission wavelength of the QW is adjusted with separate photoluminescence (PL) calibration samples that comprise only the active region of the laser structure. The room-temperature QW PL emission measured through the PL sample epistructure is targeted at slightly shorter wavelength than the operation wavelength (e.g. in the 777–778 nm range for a 780 nm operation wavelength) in order to compensate for the combination of emission wavelength blue-shift induced from post-growth annealing treatment and heat-induced red-shift induced during the laser operation.

Silicon and beryllium have been used as n- and p-type dopants, respectively, and the electron and hole concentrations have been calibrated by using the Hall method [83] on thick bulk doping samples. It has to be underlined that, due to the need for careful calibrations, the total amount of samples grown can easily reach a high multiple of the amount of grown final laser structures.

One of the epilayer structures used for the fabrication of 780 nm narrow linewidth LDs with surface gratings, including the nominal target doping concentrations, is given in Table 5.1.

The doping levels next to the heterointerfaces in high bandgap layers are targeted to be lower than the doping levels in the low bandgap layers across the heterointerfaces in order to reduce energy level notches and improve carrier flow over the potential barriers. The cladding layers' doping was linearly varied so that it is higher in regions with low optical field intensity and lower in regions with high optical field intensity.

**Table 5.1:** Epitaxial layer structure for 780 nm DFB lasers with LC-RWG surface gratings.

No.	Material	Description	Thickness (nm)	Doping ( $\text{cm}^{-3}$ )
1	GaAs	Buffer	200	$n=5 \cdot 10^{18}$
2	$\text{Al}_{0.2}\text{Ga}_{0.8}\text{As}$	Barrier reduc.	50	$n=2.5 \cdot 10^{18}$
3	$\text{Al}_{0.5}\text{Ga}_{0.5}\text{As}$	Cladding	1000	$n=1.5 \cdot 10^{18} \rightarrow 1 \cdot 10^{17}$
4	$\text{Al}_{0.35}\text{Ga}_{0.65}\text{As}$	Waveguide	300	–
5	$\text{Al}_{0.09}\text{Ga}_{0.91}\text{As}$	QW	8	–
6	$\text{Al}_{0.35}\text{Ga}_{0.65}\text{As}$	Waveguide	300	–
7	$\text{Al}_{0.5}\text{Ga}_{0.5}\text{As}$	Cladding	1000	$p=1.0 \cdot 10^{17} \rightarrow 1.5 \cdot 10^{18}$
8	$\text{Al}_{0.2}\text{Ga}_{0.8}\text{As}$	Barrier reduc.	50	$p=2.5 \cdot 10^{18}$
9	GaAs	Contact	200	$p=1 \cdot 10^{19} \rightarrow 5 \cdot 10^{19}$

**Table 5.2:** Epitaxial layer structure for 1180 nm DBR lasers with ET-RWG surface gratings.

No.	Material	Description	Thickness (nm)	Doping ( $\text{cm}^{-3}$ )
1	GaAs	Buffer	200	$n=6.6 \cdot 10^{18}$
2	$\text{Al}_{0.25}\text{Ga}_{0.25}\text{As}$	Cladding	1300	$n=4.5 \cdot 10^{18} \rightarrow 1.0 \cdot 10^{17}$
3	GaAs	Waveguide	500	–
4	$\text{Ga}_{0.66}\text{In}_{0.33}\text{N}_{0.05}\text{As}$	QW	7	–
5	GaAs	Waveguide	500	–
6	$\text{Al}_{0.25}\text{Ga}_{0.25}\text{As}$	Cladding	1200	$p=1.0 \cdot 10^{17} \rightarrow 4.0 \cdot 10^{18}$
7	GaAs	Contact	200	p++

## 5.2 Post-growth rapid thermal annealing

Post-growth thermal annealing is frequently used in order to reduce the defect densities, particularly for epiwafers grown by solid-source MBE, in which intrinsic defects (i.e. vacancy, interstitial and substitutional defects) dominate. Prior to the post-growth thermal annealing the epitaxially grown epiwafers have been covered with 200 nm of  $\text{SiO}_2$ . This layer significantly reduces the out-diffusion of arsenic during thermal annealing. However, it is known that  $\text{SiO}_2$  promotes Ga vacancies in the epilayer structure and, therefore, other options such as silicon nitride or blank GaAs wafers would be better suited for capping. Different annealing conditions were compared, targeting devices with the lowest possible threshold current and the highest possible slope efficiency. The comparisons between annealed and not annealed samples have indicated that, although the annealing might improve the laser characteristics, the epilayer structure and the initial quality of the epiwafers are the most important factors influencing the laser characteristics. Since rapid thermal annealing also smooths the abrupt heterointerfaces, it has also a significant effect on the emission wavelength, which complicates the alignment of the operation wavelength with the target emission wavelength. Due to these aspects, the rapid thermal annealing was not employed in the final device fabrication runs.

### 5.3 LC-RWG grating fabrication stages

The main stages of LC-RWG grating fabrication: the soft and flexible UV-NIL stamp fabrication, the UV-NIL imprinting, the lift-off and the LC-RWG grating etch are illustrated in the following figure and are presented in more detail in the following sub-sections.

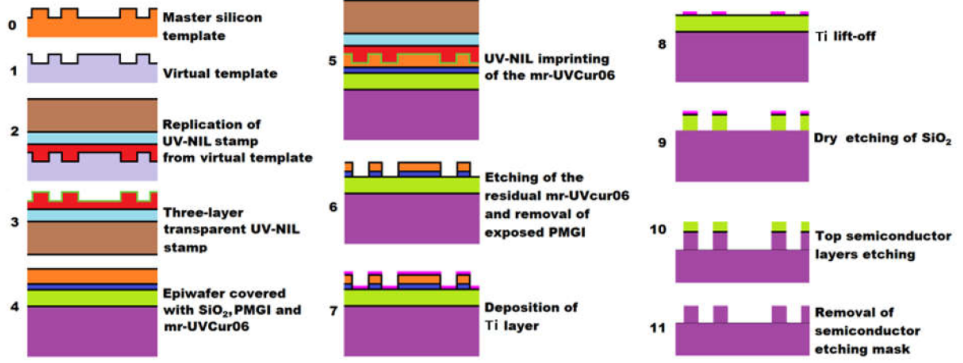


**Figure 5.1:** The process stages of LC-RWG grating fabrication. The dimensions are not to scale.

#### 5.3.1 Soft stamp fabrication

In the first stage of LC-RWG fabrication a silicon master template with the profile of the LC-RWG grating is fabricated using electron beam lithography (panel 0 of Figure 5.1). Then a virtual template with inverted LC-RWG profile is fabricated (panel 1 of Figure 5.1). The virtual template is used to obtain an UV-NIL stamp (panel 2 of Figure 5.1). Multiple UV-NIL stamps can be produced from the same master and virtual templates.

The UV-NIL stamps have to be soft and flexible to accommodate non-flat epiwafers and possible residual particles on the surface to be imprinted without breaking the brittle epiwafers, critically damaging the stamp or compromising the imprinting process. A three layer stamp structure, containing a thin hard PDMS layer with the profile to be imprinted (red layer in panel 3 of Figure 5.1), a thin 150  $\mu\text{m}$  glass sheet to prevent lateral deformation during imprint (blue layer in panel 3 of Figure 5.1) and a thick soft PDMS cushion layer (brown layer in panel 3 of Figure 5.1), is made on a glass substrate to provide both softness and flexibility in the imprinting process. The surface of the UV-NIL stamp is coated with an anti-adhesion layer (thin green layer in panel 3 of Figure 5.1) to enable stamp lifting after imprinting without damaging the imprinted UV-NIL resist.

#### 5.3.2 UV-nanoimprint and lift-off

Following the silicon dioxide ( $\text{SiO}_2$ ) layer deposition, the epiwafer surface is prepared for imprinting by successively spinning a layer of polymethylglutarimide (PMGI), which is used as a lift-off material, and then a layer of UV-curable nanoimprint resist (mr-UVCur06) (panel 3 of Figure 5.1 and panel 1 of Figure 5.2). The profile of the LC-RWG grating structure is transferred from the stamp to the mr-UVCur06 NIL-resist by pressing the stamp against the sample using 500 mbar pressure (panel 2 of Figure 5.2). The softness and flexibility of the stamp distributes the pressure uniformly across the imprinted area. The



mr-UVCur06 UV-NIL resist is cured by exposing the sample for 2 minutes to UV-light having the intensity of  $8 \text{ mW/cm}^2$ .

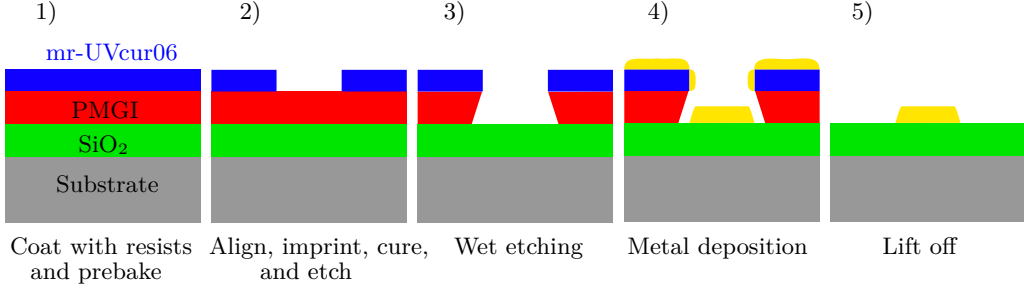


**Figure 5.2:** The process flow of the bi-layer lift off.

The residual layer of NIL resist left below the imprinted areas is dry etched using reactive-ion etching (RIE) and O<sub>2</sub>-plasma. The exposed PMGI areas are removed by wet etching leaving the inverted LC-RWG grating pattern of mr-UVCur06 and PMGI layers (panel 3 of Figure 5.2). Then a thin 50 nm titanium layer is evaporated on top of the surface of the sample (panel 4 of Figure 5.2). By lifting off the titanium from the regions where mr-UVCur06 and PMGI still cover the SiO<sub>2</sub> layer, the original LC-RWG grating profile is copied to the titanium mask (panel 5 of Figure 5.2).

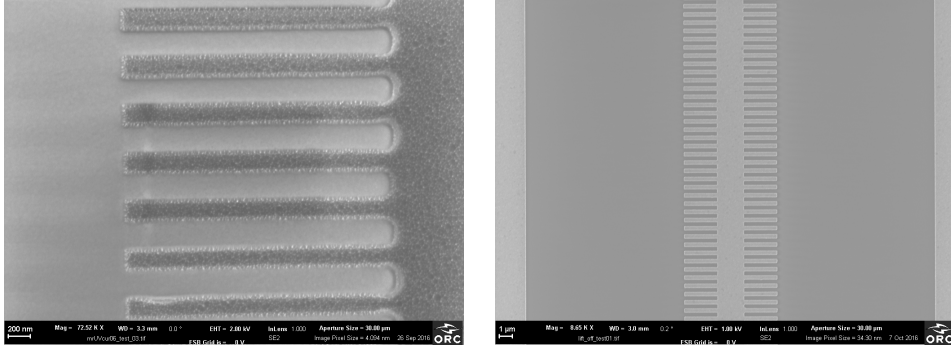


**Figure 5.3:** Top view SEM image of nanoimprinted surface gratings after the residual mr-UVCur06 resist layer is removed and the PMGI layer is wet etched (left panel) and top view SEM image of a LC-RWG structure after the lift off (right panel).

### 5.3.3 Grating etching

Using the Ti mask, the SiO<sub>2</sub> layer is dry etched by RIE and trifluoromethane (CHF<sub>3</sub>)/Ar-plasma, replicating the original LC-RWG structure pattern (protected by titanium) into SiO<sub>2</sub> (panel 9 of Figure 5.1). The inductively coupled plasma reactive ion etching (ICP-RIE) etching of GaAs/AlGaAs is subsequently performed by Cl<sub>2</sub>/N<sub>2</sub> at a low pressure (4.5 mtorr) and 45 °C, using the Ti/SiO<sub>2</sub> mask, in order to achieve a smooth semiconductor etching profile (panel 10 of Figure 5.1). During the ICP-RIE etching the Ti layer and part of the SiO<sub>2</sub> layer are also removed. Finally, the remaining SiO<sub>2</sub> is stripped off from

the top of the semiconductor LC-RWG grating profile with  $\text{CHF}_3/\text{O}_2$ -plasma dry etching (panel 11 of Figure 5.1). The left panel of Figure 5.4 shows a SEM view of the 10 nm titanium and  $\text{SiO}_2$  layers after the  $\text{CHF}_3/\text{Ar}$ -plasma etch (corresponding to panel 9 of Figure 5.1). The right panel of Figure 5.4 shows a SEM perspective view of an etched LC-RWG grating.

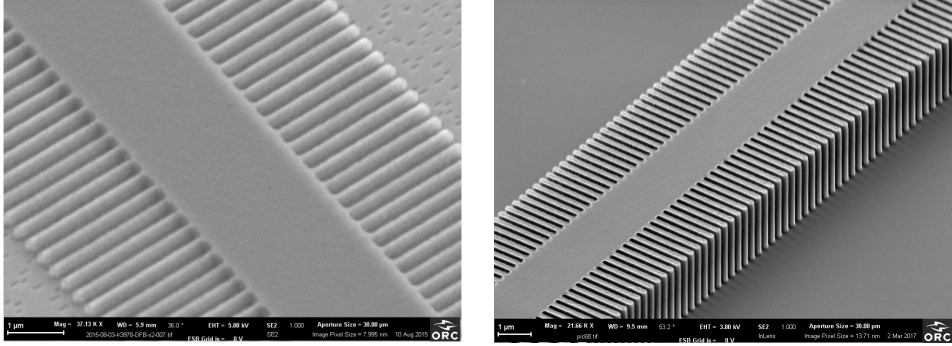


**Figure 5.4:** Top view SEM image of the  $\text{SiO}_2$  and metal mask on an epiwafer before the ICP-RIE etching (left panel) and top view SEM image of the grating structure after the etching is completed.

Due to the fundamental differences between DFB and DBR lasers, the etching steps of these device structures have many differences, as presented in [Pub2], [Pub3] and [Pub4].

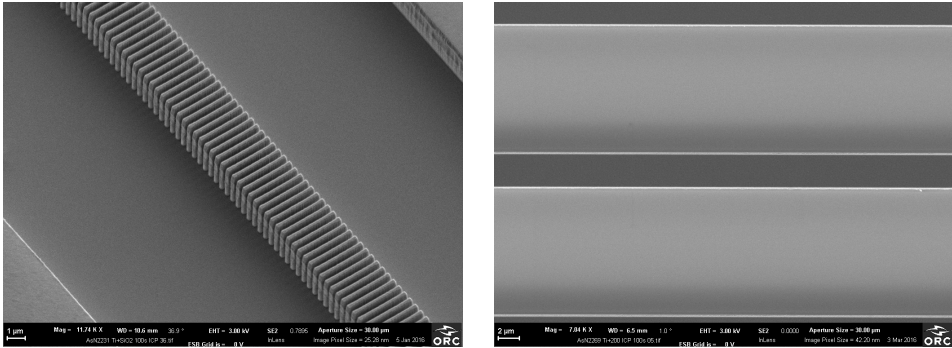


**Figure 5.5:** Top view SEM image of the ET-RWG structure of a DBR laser grating section after ICP-RIE etching (left panel) and top view SEM image of the etched RWG of a DBR laser gain section (right panel).

Since DBR lasers have essentially more sections than one (having separate gain and feedback sections), which have different etching rates and possibly different etch depth targets, the semiconductor etching of the DBR lasers is usually carried out at least in two etch steps. In the first etch step both the RWG gain section and the ET-RWG grating section(s) are etched simultaneously until the RWG section reaches the (usually shallower) target etch depth. Then the RWG section is protected by an UV-resist and the grating section(s) etching is completed in the second etch step, using the same or a different etch

recipe. The two step etching process complicates the device fabrication and makes the structure more sensitive to defects and contamination.

DBR lasers can utilize either LC-RWG or ET-RWG gratings. Because they are etched laterally through the whole ridge waveguide, the ET-RWG gratings enable a higher coupling coefficient but they also make the implementation of the grating section p-side contact problematic or even impossible. If ET-RWG gratings are employed and the BCB planarization does not flatten the structure well enough, the metal layer stack of the p-side is likely to be brittle and therefore susceptible to mechanical stress. In the worst case the metal contact layer can also reach the high intensity region of the fundamental transverse mode. Because metals are non-saturable absorbers, this would introduce significant optical absorption losses, which would eventually degrade the device performance.

## 5.4 Planarization and contact openings

After the LC-RWG (or ET-RWG) grating structure is etched into the top semiconductor epilayers, the structure is planarized by spinning BCB on the epiwafer and dry etching the excess thermally cured BCB to the level of the ridge with sulfur hexafluoride ( $\text{SF}_6$ )/ $\text{O}_2$ -plasma. Although BCB is known to have good polarization properties, it also has a low dielectric constant, which guarantees a relative good optical contrast to the semiconductor lateral protrusions of the LC-RWG grating or to the semiconductor ridge slices of the ET-RWG grating.

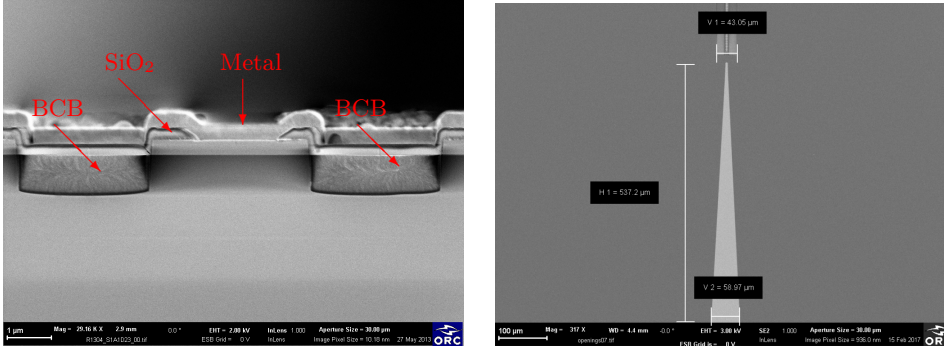


**Figure 5.6:** SEM picture of the end facet of a RWG structure after BCB planarization, opening the isolating  $\text{SiO}_2$  layer, and p-side metal evaporation (left panel) and SEM picture from a MOPA laser after the openings are etched into the  $\text{SiO}_2$  layer by RIE (right panel).

Once the structure is planarized, a 200 nm  $\text{SiO}_2$  layer is grown on top of it. Since the main task of this  $\text{SiO}_2$  layer is to enable directing the electric current flow to the selected gain regions, p-side contact openings are made into it, on top of the central ridge of width  $W$ . In the same lithography step the openings are made for the flared top contact of the semiconductor optical amplifier section when MOPA lasers are fabricated.

Because the high aspect ratio LC-RWG grating cannot be exposed to wet etching due to the possibility of damage, the patterning of the contact openings uses standard contact UV-lithography performed with an i-line mask aligner. The following contact opening patterning steps have been employed:

- a positive photoresist is deposited on the sample and is exposed at the top of the ridge,
- the resist is developed,
- the  $\text{SiO}_2$  is removed from the developed narrow opening using  $\text{CHF}_3/\text{Ar}$ -plasma,
- the remaining resist layer is removed using a *n*-methyl pyrrolidone (NMP)-based stripper.

## 5.5 p- and n-side metalization

The p-side is metalized in order to provide ohmic contact to the anodes of the master oscillator section and of the optical amplifier section. The p-side contacts are evaporated simultaneously for all the LD sections. A standard p-type metalization, consisting of 50 nm titanium, 50 nm platinum and 250 nm gold, has been used. The metalization method should either be conformal enough to follow the sidewalls of the ridge or the sample should be properly tilted. Failure to meet these criteria can jeopardize the contact quality.

The p-side metal can also be patterned, although this is not always mandatory for single contact devices. However, due to practical reasons, it is good to electrically isolate the p-contacts of adjacent LDs because it enables on-the-bar probing. Markings on p-metal, produced by patterning, can also be used to recognize different types of emitters placed on the same processed sample. In addition the markings can also be used to indicate the direction of emission from AR/HR coated emitters and to provide alignment marks for automated packaging, if needed. The p-side metal patterning is made using image reversal lithography in i-line mask aligner. The standard operating procedures of AZ5214E image reversal resist are followed.

Following p-side metalization, the wafers are thinned in order to enable good quality cleaving of the LD facets. Chemical mechanical polishing (CMP) is typically used for wafer thinning. Alumina-containing slurry is employed to grind the wafer to the thickness of 130  $\mu\text{m}$  in a first step. Another 20  $\mu\text{m}$  are subsequently removed with sodium hypochlorite ( $\text{NaClO}$ )-based chemical polishing fluid. This leaves a polished, damage free surface on the n-side of wafer.

The n-side ohmic contacts of the LDs are evaporated on the polished n-face of the wafer. The metal stack contains a 5 nm thick nickel adhesion layer, a 5 nm thick gold wetting layer, a 30 nm thick germanium layer and finally a 90 nm thick gold layer. This metal layer stack is annealed at 370  $^\circ\text{C}$  for 60 s in order to form a AuGe-alloy that diffuses into the n-GaAs contact layer. The diffusion helps the formation of a high quality ohmic contact.

## 5.6 Dicing and mounting

The wafers have been diced using the standard operating procedures for edge emitting laser diodes. First the cleaving planes are initiated by using a diamond scribe, then facets are cleaved and bars are formed. Typically the formed laser bars are about 8.5 mm long, containing multiple emitters whose lengths may vary depending on requirements.

Subsequently, the laser bars are mounted on a holder that is loaded on an electron beam evaporator. For edge emitting DFB and DBR lasers HR- and AR-coatings are usually

evaporated on the end facets. HR-coatings, if used, are evaporated on the non-emitting facet of the laser, whereas AR-coatings can be applied on both facets.

A HR-coating comprises a stack of alternating quarter-wavelength thick layers of non-absorbing dielectrics that have a relatively high refractive index contrast such as titanium dioxide ( $\text{TiO}_2$ ) and  $\text{SiO}_2$ , while multi-layer AR-coatings are typically made of material layers having a refractive index value profile that increases towards the cleaved semiconductor interface. Single layer AR-coatings consist of a quarter-wavelength thick layer of a dielectric material with a low refractive index (preferably as close as possible to the square root of the product between the output medium refractive index and the effective refractive index at the emitting end of the LD). Multi-layer AR-coating structures can reach lower reflectivities and are less sensitive to refractive index or thickness variations. On the other hand, as the thickness of the coating increases, there is a higher risk that it peels off under mechanical stress or vibrations. After coating, the bars are unmounted from the bar holder and mounted back to the diamond scribe. Subsequent scribing is used to separate the bars into individual emitters.

Particularly for MOPA lasers the thermal management is a crucial issue since at higher injection currents more heat is generated in the active region, particularly in the SOA section, due to the ohmic heating. The heating can degrade the device performance and limit the output power of the laser or even prevent the device from lasing [84]. This problem can be alleviated by minimizing the threshold current, internal losses, carrier leakage, non-radiative recombinations, and by optimizing the doping profile. The heat dissipation from the active region can be improved by decreasing the thermal resistance between the active region and the heat sink.

Since the processed p-side side is much thinner than the n-side, which includes the substrate, the thermal resistance is smaller for the p-side than for the n-side. Hence, p-side down mounting onto a submount/heat sink usually improves device characteristics and increases the roll-off power. Because the p-side is only a  $1\text{--}2\text{ }\mu\text{m}$  thick, the thickness of the solder layer must be very thin to avoid short-circuiting the active region. Therefore, (semi-)automated mounting equipments are used to prevent the short circuits and provide mechanically, electrically, and thermally good contact between the laser chip and the submount/heat sink. The heat conductivity can be increased by widening and lengthening the dimensions of the p-side opening, but these dimensions may be restricted due to the increased far-field asymmetry of the output beam or gain saturation and poorer efficiency, for example.

## 5.7 Fabrication limitations

Even though complex surface grating structures can be manufactured by the sequence of stages described in the previous sections, the presented fabrication method still has various limitations that affect the device performance, and the reproducibility of the results, as well as the fabrication yield and throughput.

Since the UV-NIL is capable of defining very small half pitches, in the range of  $12.5\text{--}50\text{ nm}$  [35, 36], with an overlay accuracy of  $\sim 20\text{ nm}$  [37], the fabrication method should enable fabricating down to first order gratings for DBR or DFB lasers covering the whole visible wavelength range. However, because the gratings are usually etched down from the contact layer close to the interface between the cladding and the waveguide in order to get sufficient optical feedback, the low-order grating structures require a high etch aspect ratio (i.e. the ratio between the etch depth and the grating trench width) for

short wavelengths. Short period surface gratings, having rectangular high aspect ratio features, almost perfectly vertical sidewalls, low surface roughness and uniform etch depth with repetitive protrusion and trench profiles are difficult to etch since this requires high anisotropy.

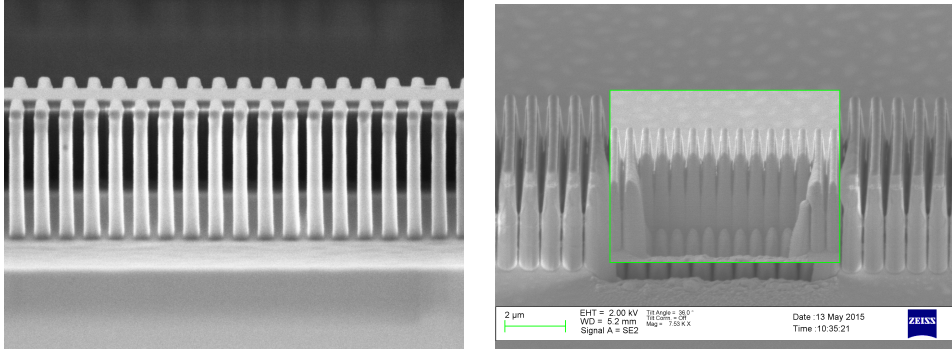


**Figure 5.7:** (Left panel) Side view SEM image of a 3<sup>rd</sup>-order LC-RWG grating structure with 1250 nm etch depth and  $\sim 350$  nm grating period, after ICP-RIE etching. The etch parameters have been:  $+45$  °C temperature, 4.5 mtorr pressure, 80 W platen power, 500 W coil power, and  $\text{Cl}_2/\text{N}_2$  gases with a 20/2.5 sccm flow ratio. (Right panel) Side view FIB-SEM image of a 3<sup>rd</sup>-order ET-RWG grating with a v-shaped trenches. The grating profile does not require very good sidewall verticality and, therefore, it simplifies the etching, but leads to a reduction in the grating coupling coefficient.

In general highly anisotropic dry etching is obtained by increasing the ion bombardment but the associated sputtering is non-selective and allows the redeposition of the etched byproducts. Because of the non-selectivity, the etch rate of the mask, which is usually made of  $\text{SiO}_2$  or silicon nitride, and the etch rate of the epilayer structure are relative close to each other. This usually means that the etch mask should be thick in order to prevent the mask from wearing out, but thick high quality etch masks are more difficult to fabricate. Moreover, thick masks promote shadowing effects and can influence the width of the gratings lines (i.e. the grating filling factor). High energy ions also induce high surface damage and roughness. Hence, lower energy ions are favored, but this diminishes the etch rate, which is required to be high in commercial device fabrication processes. The lower etch rate can be compensated by a higher ion flux.

The erosion of the etch mask can be decreased by chemical/reactive etching. Chemical etching is very selective which improves the etch rate [85] but it is isotropic. Isotropic etching is not directional and thus it can affect the sidewall verticality. Hence, a very carefully controlled balance between the etch process parameters such as the etching temperature and pressure, the flows of the enchants and diluting agents, passivation, the ion acceleration voltage, and the plasma density is needed to obtain a good etch profile.

A high-aspect ratio and short grating period induce aspect ratio dependent etching (ARDE) and microloading effects [86–88]. Microloading is related to the lower etch rates observed in high feature density areas, while ARDE is referring to the effects leading to lower etch rates in narrow trenches. Microloading is caused by localized depletion of reactive species or accumulation of the etching byproducts [88]. Several mechanisms have been proposed to explain the ARDE effect, among which are:

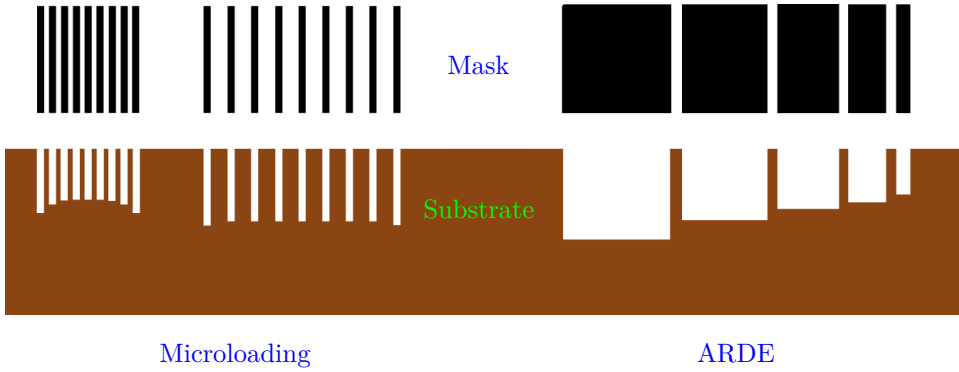


**Figure 5.8:** Illustration of microloading and ARDE effects.

- Knudsen transports of neutral radicals (i.e. some neutrals are deflected from the sidewalls of the trenches without a reaction) [89],
- ion and neutral shadowing (i.e. the fluxes of enphants are blocked or deflected by the etch mask and the sidewalls) [90],
- charging effects (i.e. ions can be deflected or decelerated due to electrostatic forces caused by the charge density distribution on insulating surfaces) [91].

ARDE induces un-etched pockets at the bottom of the grating trenches towards the central ridge, exactly in the regions where the gratings should mostly be coupled to the optical field. A larger lateral extension of the grating protrusions reduces the ARDE effect and the un-etched pockets but induces greater lateral current leakage through the lateral protrusions.

The etching-depth-dependent etch rate associated with ARDE has also been mitigated by adjusting the etch parameters such as the pressure, the gas flow rates, and the platen power [92]. A small fraction of oxygen [93] and the ramping of etch parameters [94] are also used to compensate the ARDE effect and enable the etching of very high aspect ratio features. However, the combination of a high aspect ratio, short period, deep smooth and vertical grating trenches and high anisotropy is difficult to obtain. Consequently, the grating etch step usually limits the smallest attainable period for rectangularly shaped gratings with a given filling factor and target etching depth.

An increase in the grating trench width or a smaller etch depth improve the gas flows, enhancing also the etch rate in narrow trenches, but these geometrical changes also affect the grating coupling, the Bragg resonance wavelength or the grating order. A grating structure, where the grating protrusions are alternately placed on one and the other side of the ridge [Pub4] has been used in this thesis in order to alleviate the etch limitations. The experiments have shown that similar coupling coefficients, trench widths and Bragg resonance wavelengths as for LD-RWG gratings with protrusions placed symmetrically on both sides of the central ridge can be obtained with lower order gratings having the protrusions alternately placed on the sides of the central ridge [Pub4]. Alternately placed lateral protrusions also enable an improved carrier injection and lower lateral current spreading to the areas where the light intensity is low and the carriers are rather wasted to

spontaneous or non-radiative recombinations than used in stimulated emission. Moreover, lower order gratings also have lower radiative losses [95].

Because the grating protrusions must be relatively long in the lateral direction to ensure a sufficient coupling coefficient, the lateral extension of the grating protrusions ( $D$ ) cannot be much smaller than the ridge width ( $W$ ). Furthermore, a wider lateral extension of the protrusions prevents the formation of shoulders in the transverse grating profile (see Figure 5.9), close to the high optical field intensity region below the ridge. Moving the etch interfaces away from high optical field intensity areas is important because the etched interfaces can promote surface states that act as recombination centers for spontaneous emission and non-radiative recombinations.

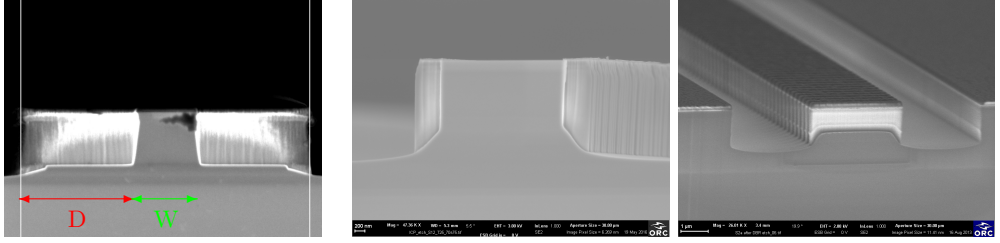


**Figure 5.9:** (Left panel) SEM view of a cleaved end facet of a DFB laser with LC-RWG gratings having a relatively wide ( $W=1.4\mu\text{m}$ ) central ridge and a large lateral extension of the protrusions ( $D=2.5\mu\text{m}$ ), after ICP-RIE. (Middle panel) SEM view of a cleaved end facet with otherwise similar gratings but with a  $W=2.5\mu\text{m}$  wide central ridge and a  $D=0.5\mu\text{m}$  lateral extension of the protrusions. (Right panel) SEM view of an end facet cleaved through the DBR laser section with rectangular ET-RWG gratings, showing that ET-RWG gratings also suffer from ARDE and microloading effects, resulting in a smaller etch depth through the ridge than in the open area.





# 6 Device characterization results

## 6.1 DFB characterization results

The light-current-voltage (LIV) characteristics of anti-reflection (AR) coated ( $< 1\%$  reflectivity) DFB lasers were first measured on bar with a bar probe to identify the devices with the good characteristics (usually around 50 % of the chips had good characteristics). The bars were then diced and the chips having good characteristics were mounted and wire bonded. The mounted DFBs were then measured for their LIV characteristics. It was found that most devices that were mounted and bonded had a good voltage behavior, but, possibly due to mounting and bonding inaccuracies (e.g. mounting voids and/or contact non-uniformities), many devices exhibited light-current (LI) characteristics indicating multi-mode operation or mode hops. As a result, only  $\sim 20\%$  of the initial devices were mounted, bonded and selected for further detailed characterization. It should be underlined that this yield of fully characterized devices is reasonably good, taking into account that both the device structures and the fabrication technology have been developed largely during this work.

The mounted and bonded DFB lasers with good LIV characteristics were measured for their spectra over a bias range from threshold current to 300 mA. The 300 mA upper limit was chosen with a safety margin since the corresponding output power was enough for the input of the PA SOA section and because at around 600 mA to 700 mA bias current some of the DFB chips failed (likely mainly due to poor thermal management associated with p-side-up mounting) and failures could destroy some good devices. The measured spectra were used to determine the individual chips with a broad single mode emission range. For those chips the linewidth was measured with a delayed self-heterodyne interferometric technique at 20 °C.

The left panel of Figure 6.1 shows LIV characteristics of a typical 2.4 mm long DFB laser with 3<sup>rd</sup>-order symmetric LC-RWG gratings (having the epilayer structure described in Table 5.1 and  $t=50$  nm,  $W=2\text{ }\mu\text{m}$ ,  $D=2\text{ }\mu\text{m}$ ) measured in continuous wave CW operation mode at 20 °C. The threshold current and opening voltage are 118 mA and 1.59 V, respectively. The series resistance is around  $0.62\text{ }\Omega$  and the slope efficiency per facet is about  $0.15\text{ mW/mA}$  above the threshold current and below the output power saturation. An output power of 28.9 mW was obtained for a 300 mA bias current.

The right panel of Figure 6.1 shows several LI curves of another typical 2.4 mm long DFB laser with 3<sup>rd</sup>-order symmetric LC-RWG gratings (having the epilayer structure described in Table 5.1 and  $t=50$  nm,  $W=2\text{ }\mu\text{m}$ ,  $D=2\text{ }\mu\text{m}$ ), measured at heat sink temperatures varying from 25 °C to 50 °C. The measurements were carried out in pulsed mode (with 1  $\mu\text{s}$  pulse width and 1 % duty cycle) to minimize the effects of mounting thermal resistance on the laser performance. The measured threshold current increase with heat sink tempera-

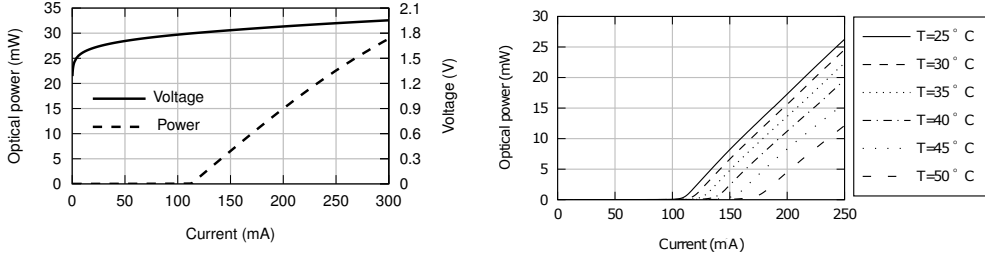


**Figure 6.1:** Continuous wave LI (dashed line) and VI (solid line) characteristics of a DFB laser at 20 °C (left panel) and pulsed mode LI-characteristics of a DFB laser at different heat sink temperatures (right panel). The measurement pulse width was 1  $\mu$ s and the duty cycle was 1%. The lasers are 2.4 mm long and have a 3<sup>rd</sup>-order symmetric LC-RWG grating with  $t=50$  nm,  $W=2$   $\mu$ m and  $D=2$   $\mu$ m.

ture was: 110 (25 °C), 117 (30 °C), 127 (35 °C), 138 (40 °C), 155 (45 °C), 176 (50 °C) mA while the measured slope efficiency decreased from 0.18 mW/mA to 0.15 mW/mA as the heat sink temperature was increased from 25 °C to 50 °C. The resulting characteristic temperature is somewhat poorer than for typical GaAs-based epilayers. However, it should be noted that other parameters beside the available material gain are temperature dependent, particularly the increasing carrier leakage has been shown to affect the characteristics at higher temperatures [53]. The LC-RWG gratings may be responsible for the higher-than-typical current leakage through the lateral protrusions, which does not contribute significantly to stimulated light emission but contributes to device heating. Reduced current leakage through the lateral protrusions (by employing oxide apertures and/or alternating lateral protrusions) would improve the device thermal behavior.

3<sup>rd</sup>- and 1<sup>st</sup>- order LC-RWG grating DFBs with symmetrical and alternating grating configuration, respectively, and having similar coupling strengths were fabricated from the epilayer described in Table 5.1. The devices were measured to assess the effect of the alternating grating scheme on laser performances. In the alternating grating devices the grating protrusion width in the lasing direction of the cavity ( $\Lambda_1$ ) was designed to be 85 nm and the grating trench width ( $\Lambda_2$ ) varied from 143 nm to 150 nm depending on the grating pitch. If the alternating grating scheme were not used, the corresponding grating trench width for the 1<sup>st</sup>-order symmetrical LC-RWG grating ( $\Lambda_2$ ) would have been from 29 nm to 32.5 nm. Such narrow grating trenches cannot be etched down to a 1250 nm depth with the current available technology. For the symmetrical devices  $\Lambda_1$  was varied from 147 nm to 150 nm and  $\Lambda_2$  from 196 nm to 200 nm. The calculated real coupling coefficients for the 1<sup>st</sup>-order alternating and 3<sup>rd</sup>-order symmetrical LC-RWG gratings were  $\sim 5.0$  cm<sup>-1</sup> and  $\sim 4.6$  cm<sup>-1</sup>, yielding 1.2 and 1.1 coupling strengths for the 2.4 mm device lengths, respectively.

Figure 6.2 shows a comparison between typical continuous wave LIV-characteristics measured at 20 °C for 2.4 mm long DFB lasers fabricated from the same epiwafer with 1<sup>st</sup>-order alternating and with 3<sup>rd</sup>-order symmetrical LC-RWG gratings. Figure 6.3 gives the threshold current and slope efficiency distributions determined from measuring on bar several 2.4 mm long DFB lasers: 19 devices with 1<sup>st</sup>-order alternating and 18 devices with 3<sup>rd</sup>-order symmetrical LC-RWG gratings. The measurement results have reasonably good grouping and show that the average values of the threshold and slope efficiency represent well the fabricated devices. It should, however, be mentioned that the slope efficiency

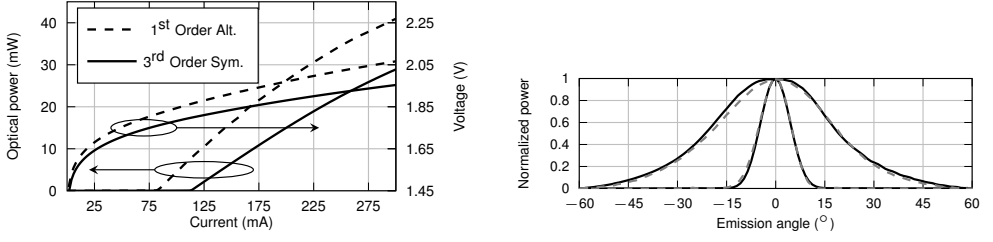


**Figure 6.2:** Comparison between the continuous wave LIV characteristics (left panel) and between far-field patterns (right panel) of the two types of DFB lasers with different LC-RWG gratings: 1<sup>st</sup>-order alternating and 3<sup>rd</sup>-order symmetrical. The device lengths were 2.4 mm. The FWHM values for fast and slow axes were 40 and 11 deg., respectively, for both type of devices. Dashed line denotes 1<sup>st</sup>-order alternating grating and solid line 3<sup>rd</sup>-order symmetrical in both panels. [Pub4] reproduced with permission.

measurements performed on bar did not yield correct well-calibrated values (particularly due to current spreading/leaking to neighboring chips). However, since all slope efficiency measurements for Figure 6.3 were done under the same conditions, the comparison yields valid conclusions.

The results shown in Figure 6.3 reveal that the devices with alternating gratings have both a higher slope efficiency and a lower threshold current but, according to Figure 6.2, they also have a higher series resistance. The series resistance increases because less injected current goes through the protrusions. Thus, the increased series resistance is actually a benefit, because the current through the protrusions does not contribute significantly to the stimulated emission.

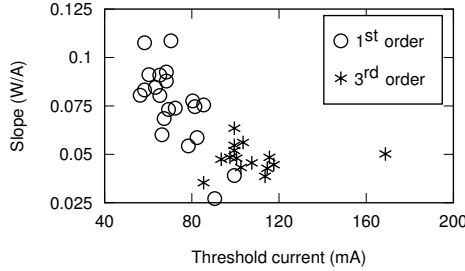


**Figure 6.3:** Slope versus threshold current for DFB lasers measured from two bars with 1<sup>st</sup>-order alternating and 3<sup>rd</sup>-order symmetrical LC-RWG gratings.

From the right panel of Figure 6.2 it is clear that the far field patterns of the two grating configuration lasers are almost identical. This also means that the near field profiles are almost the same. The lack of kinks in the far field patterns indicates that the lasers operate in single transverse mode regime. These results indicate that as long as the design of the alternating grating structure is properly done, it has negligible effect on the single transverse mode performance of the laser.

The emission wavelength of the symmetrical and alternating grating devices changes with current at a rate of 5.5 and 5.1 nm/A, respectively, as illustrated in Figure 6.4. The higher

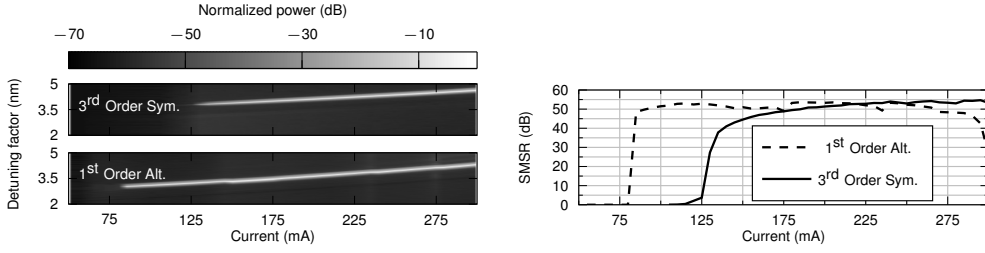


**Figure 6.4:** Variation of the optical spectra (left panel) and of the SMSR (right panel) with bias current for 2.4 mm long DFB lasers having a 3<sup>rd</sup>-order symmetrical and 1<sup>st</sup>-order alternating LC-RWG gratings. [Pub4] reproduced with permission.

rate of change in the emission wavelength indicates that the devices with symmetrical gratings heat up more when biased, which results from the fact that a higher amount of current is diverted through the lateral protrusions. Figure 6.4 also shows that the two types of devices have similar detuning factors (the difference between the emission wavelength and gain maximum), which means that the difference in performances between the DFB lasers with different types of gratings is not due to better gain alignment with the grating Bragg resonance. The results presented in Figures 6.2 and 6.4 show that when the 1<sup>st</sup> order alternating grating DFBs are well designed, they result in a broad and stable single transverse and single longitudinal mode operation domain with high SMSR. Taking into account the lower thresholds and higher slope efficiencies, the alternating grating scheme provides a clear improvement to the overall performance of LC-RWG DFB lasers.

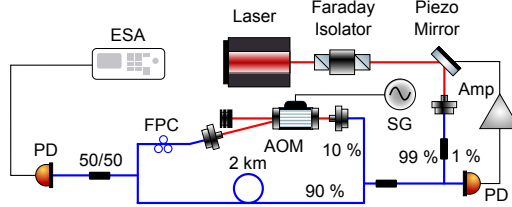


**Figure 6.5:** The self-heterodyne linewidth measurement system that was used to determine the emission spectral linewidth for the devices under test.

Because the linewidths of the fabricated lasers are much smaller than the resolution of the available optical spectrum analyzers, the phase noise characterization has been carried out using more accurate and stable RF instruments and an interferometric measurement system. The interferometric delayed self-heterodyne setup shown in Figure 6.5 was used for determining the linewidth of the DFB lasers. The delay line in the self-heterodyne measurement setup was a 2 km single mode fiber with 2.8 dB/km attenuation. The acousto-optic modulator was used to shift the other arm of the interferometer in frequency (with 200 MHz) to avoid the low frequency noise of the photodiode and of the spectrum analyser. Since a subcoherence heterodyne signal was obtained from the measurements, it was determined that the delay line length of 2 km was not enough to completely decorrelate the two beams. For instance, a 10 kHz laser linewidth corresponds to a coherence length of  $L_{\text{coh}} = \frac{c/n_{\text{eff}}}{\pi \cdot \Delta\nu} \approx 6.5 \text{ km}$  in the delay fiber. Taking into account that for good enough decorrelation the delay fiber should be much longer than the coherence length, a long

enough delay fiber would result in very high losses in the delay arm of the interferometer. As an example, a 10 km long fiber would itself induce 28 dB attenuation and with coupling losses the attenuation would be well above 30 dB. Since an electrical amplifier with low enough noise was not available to be used after detection, a long enough fiber for decorrelation was not feasible.

Consequently, a power spectral density (PSD) formula derived for delayed self-heterodyne interferometer taking into account only the white noise of the laser [96, 97] was used to fit the measured PSD spectra. According to this white noise model, the PSD for the detector current generated by the beat signal is [96–98]:

$$S(\omega) = E_0^4 \left\{ (1 + \alpha^2)^2 \delta(\omega) + 2\alpha^2 \exp(-S_0 \tau_{delay}) \delta(\omega - \Omega) + 2\alpha^2 \frac{2S_0}{S_0^2 + (\omega - \Omega)^2} \cdot \left[ 1 - \exp(-S_0 \tau_{delay}) \cdot \left( \cos[(\omega - \Omega) \tau_{delay}] + \frac{S_0}{\omega - \Omega} \sin[(\omega - \Omega) \tau_{delay}] \right) \right] \right\}, \quad (6.1)$$

where  $\omega = 2\pi\nu$  is the angular frequency,  $\Omega$  is the modulation angular frequency of the acousto-optic modulator, and  $\Delta\nu = S_0/(2\pi)$  [Hz] is the FWHM intrinsic linewidth. In Equation (6.1)  $E_0$  is the optical field amplitude,  $\alpha$  is the amplitude ratio of the interfering optical fields,  $\delta$  is the delta function, and  $\tau_{delay}$  is the time delay between the interfering optical fields. The emission linewidth was evaluated as the linewidth value used in the PSD formula that resulted in the best fit with the measurement results.

The left panel of Figure 6.6 gives an example of the measured power spectrum of the detector current generated by the interferometer beat signal for 185 mA bias current applied to a 2.4 mm long DFB laser with 1<sup>st</sup>-order alternating LC-RWG gratings fabricated out of an epiwafer with the structure defined in Table 5.1. The best fit between the theoretical model for the PSD given by Equation (6.1) and the measured data was obtained with a  $\Delta\nu = 3.9$  kHz linewidth. The linewidth, amplitude and attenuation were used to fit the model to the measurements in the least squares sense. The spacing between the fit minima ( $\Delta f$ ) corresponds almost exactly to the delay time introduced by the 2 km long fiber with the refractive index of 1.4537:

$$\Delta f \approx \frac{1}{\tau_{delay}} = \frac{1}{(L_{fiber} \cdot n_{eff})/c} = 103 \text{ kHz}. \quad (6.2)$$

where  $L_{fiber}$  is the length of the fiber,  $n_{eff}$  is the effective refractive index, and  $c$  is the speed of light in vacuum.

The right panel of Figure 6.6 shows the variation of the evaluated linewidth with the bias current of the 2.4 mm long DFB laser with 1<sup>st</sup>-order alternating LC-RWG gratings for which the fitting was illustrated in the left panel. The linewidth is somehow reduced at higher bias currents but the variation has jumps and does not follow the clear narrowing trend predicted by Equations (4.3) and (4.6). It is likely that technical noise and/or re-broadening effects are responsible for the atypical linewidth variation with increasing bias current.

The emission linewidth was also measured for a 2.4 mm long AR-coated DFB laser with symmetrical 3<sup>rd</sup>-order gratings using the same measurement system. In the fitting of Equation (6.1) with the measurements for these lasers the Dirac function at the modulation

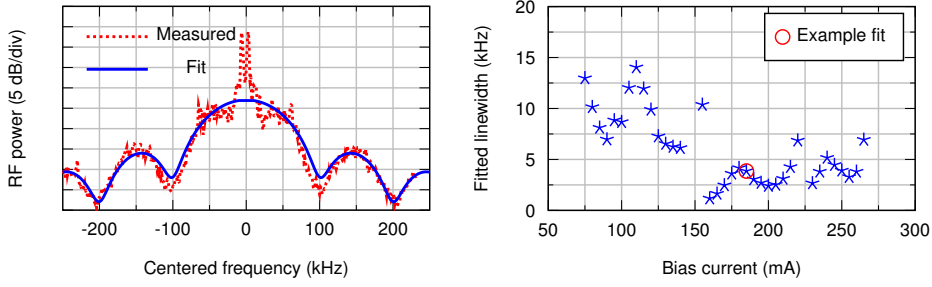


**Figure 6.6:** Measured and 3.9 kHz linewidth least-squares best fit of the power spectral density for the detector current generated by the beat signal in the interferometric delayed self-heterodyne measurement setup (left panel) and variation of the fitted linewidth with the bias current applied to a 2.4 mm long DFB laser with 1<sup>st</sup>-order alternating LC-RWG gratings ( $t=150$  nm,  $W=2$   $\mu$ m,  $D=2$   $\mu$ m) (right panel). The point in the right panel corresponding to the fit presented in the left panel is marked with a red circle.

frequency of the acousto-optic modulator was also neglected. The left panel of Figure 6.7 shows that the measured data at 300 mA bias current is well fitted by the theoretical PSD given by Equation (6.1) for a 7.4 kHz linewidth, except for the offset frequency range of  $[-0.1, 0.1]$  MHz.

Because of the imperfect fitting of the theoretical PSD given by Equation (6.1) to the measured data, a second method was used to verify the emission linewidth evaluated for the DFB lasers with symmetric 3<sup>rd</sup>-order gratings. Assuming that the PSD has the form of Equation (6.1), it has been shown that the linewidth can be directly determined from the contrast difference between the maxima and minima of the PSD [99]. The contrast difference between the second maximum and the second minimum is given by [99]:

$$\Delta S(\Delta\nu) = 10 \log_{10} \frac{\left[1 + \left(\frac{2c}{n_{eff} \Delta\nu L_{fiber}}\right)^2\right] \left[1 + \exp\left(-2\pi \frac{n_{eff} \Delta\nu L_{fiber}}{c}\right)\right]}{\left[1 + \left(\frac{3}{2} \frac{c}{n_{eff} \Delta\nu L_{fiber}}\right)^2\right] \left[1 - \exp\left(-2\pi \frac{n_{eff} \Delta\nu L_{fiber}}{c}\right)\right]}, \quad (6.3)$$

By taking the contrast difference from the measured PSD, the FWHM linewidth can be determined from Equation (6.3) if the other parameters in the equation are known. This method of using the contrast difference between the second peak and the second trough (CDSPST) is fast and requires a small amount of computational power (since the complicated least-square fitting is avoided) but it is still relying on the shape of the PSD given by Equation (6.1). The right panel of Figure 6.7 shows that the linewidths evaluated by the two methods for the DFB laser with symmetrical 3<sup>rd</sup>-order gratings are similar over the whole measured bias range.

Figures 6.6 and 6.7 indicate that even though the lasers were fabricated from the same epiwafer (having the epilayer structure given in Table 5.1), the alternating grating structure provided slightly narrower linewidth at higher bias currents. This deviation could have been induced by fabrication and measurement inaccuracies but it is more likely determined by laser characteristics' differences such as the estimated lower internal losses and lower lateral current leakage of the DFB lasers with 1<sup>st</sup>-order alternating LC-RWG gratings, as compared to their counterparts with 3<sup>rd</sup>-order symmetric gratings. The simulated real

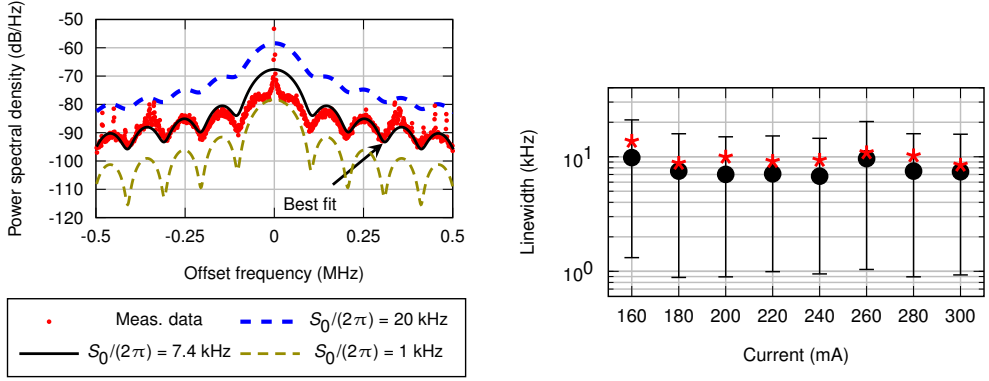


**Figure 6.7:** (Left panel) Measured PSD spectrum of a 2.4 mm long DFB laser with a symmetric  $3^{rd}$ -order grating ( $t=50$  nm,  $W=2$   $\mu$ m,  $D=2$   $\mu$ m) and theoretical PSD spectra given by Equation (6.1) for different Lorentzian FWHM linewidths. The theoretical PSD spectra have shifted power levels for illustration purposes. The measurements have been done at 20 °C with 300 mA bias current. The bandwidth resolution of the ESA was 1 kHz with the integration time of 2.5 ms. (Right panel) Linewidth FWHM variation with bias current for the same laser, extracted from Equation (6.1) fits to the measured PSD (black dots) and determined from the contrast difference between the second peak and second through of the measured PSD (red stars). The error bars indicate 95% confidence intervals for the extracted FWHM linewidths. [Pub3] reproduced with permission.

parts of the coupling coefficients were  $\sim 5$   $\text{cm}^{-1}$  and  $\sim 4.6$   $\text{cm}^{-1}$  for the fabricated 2.4 mm long  $1^{st}$ -order alternating and  $3^{rd}$ -order symmetrical gratings. Therefore, the possible small mirror loss difference (taking into account the fabrication inaccuracies and the fact that nominally the same AR-coatings were deposited on the end facets for both laser structures) is unlikely to be the main/only reason for the evaluated linewidth difference between the DFB lasers with  $1^{st}$ -order alternating and  $3^{rd}$ -order symmetrical gratings (see, for reference, the calculated linewidth variation with grating coupling coefficient and grating length shown in Figure 4.6).

For both DFB laser types, the linewidth is almost independent of the bias current. The absence of linewidth reduction with increasing bias current is likely due to re-broadening effects and/or to the fact that we have evaluated the linewidth by fitting measured PSD spectra resulted from the total linewidth (including the Gaussian contribution of the technical noise, which is not diminishing with increasing current [100] ) with the theoretical PSD spectra derived only from the intrinsic Lorentzian linewidth. Further studies are necessary for determining the why the linewidth does not narrow as the bias current is increased, according to Equations (4.3) and (4.6). The re-broadening effects should be analyzed and alleviated in case that the linewidth floor has been reached due to re-broadening effects. On the other hand, the intrinsic Lorentzian laser linewidth might be narrower than evaluated if the bias-independent technical noise is dominating the measured linewidth (and thus inducing the lack of linewidth narrowing with increasing bias current).



## 6.2 DBR characterization results

LIV, optical spectrum, and linewidth measurements have been carried out for 1180 nm DBR lasers having a 3 mm long RWG section with  $3.2\ \mu\text{m}$  ridge width and a 2 mm long unbiased ET-RWG DBR section at the non-emitting end. The epilayer structure of the 1180 nm DBR lasers is given in Table 5.2. The DBR section employed a 3<sup>rd</sup>-order ET-RWG surface grating with v-shaped trenches etched through the central ridge. The etch depths for the RWG and DBR sections were  $\sim 1440\ \text{nm}$  and  $\sim 1420\ \text{nm}$ , respectively. The end facets were AR-coated with a single quarter-wavelength thick layer of alumina giving a 2.9% reflectivity at the emission wavelength of 1180 nm.

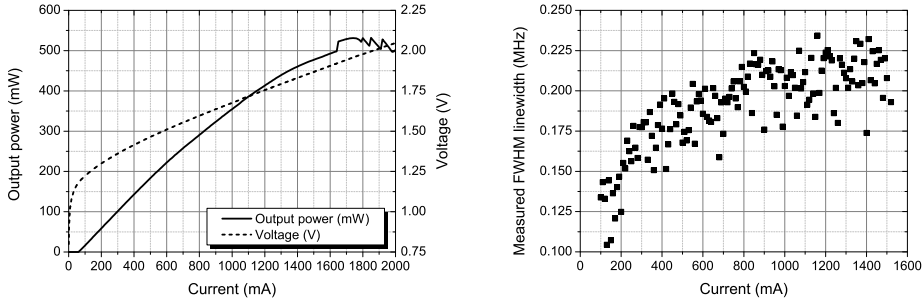


**Figure 6.8:** LIV-characteristics for a 1180 nm DBR laser with 3<sup>rd</sup>-order ET-RWG surface gratings at 20 °C (left panel). Variation of the emission linewidth with increasing bias current for the same device, measured with a delayed self-homodyne measurement setup at 20 °C. [Pub2] reproduced with permission.

The devices exhibit excellent LIV-characteristics at 20 °C, providing CW output power of  $\sim 500\ \text{mW}$  in single-mode operation for a current of 1630 mA. The measured threshold current density was  $\sim 719\ \text{A}/\text{cm}^2$ , the measured average slope efficiency was  $\sim 0.32\ \text{W}/\text{A}$ , and the series resistance was  $\sim 0.35\text{--}0.4\ \Omega$ . Strong mode hopping appears above 1630 mA and the output power saturates. The LI characteristics show no kinks or mode-hop jumps from threshold to the output power saturation point.

A delayed self-homodyne measurement setup has been used for evaluating the linewidth of 1180 nm DBR lasers targeting high-power narrow linewidth emission. In this simplified linewidth measurement system the acousto-optic modulator is removed, which can affect the measurement accuracy by introducing more noise to the measured PSD. The linewidth measurement were performed at 15 °C. The linewidth was evaluated for increasing bias currents by fitting in the least-squares sense a Lorentzian lineshape to the spectra measured by the electrical spectrum analyzer (ESA). The frequency resolution was 8.7 kHz. The results, shown in the right panel of Figure 6.8, point out that the emission linewidth for the 1180 nm DBR lasers is kept below 250 kHz in the entire the current range from 0 mA to 1630 mA. The evaluated linewidth broadens as the bias current increases, which implies that the DBR lasers suffer from re-broadening effects that overcome the emission linewidth narrowing with increasing bias current. It should be noted that the Equations (4.3) and (4.6) are derived for DBR lasers which are above transparency in all regions of the cavity. In multi-section lasers, such as DBR lasers with a passive reflector, the above transparency assumption does not hold and it is expected that there is a difference between the linewidth value predicted by the model and what is actually

measured. It is difficult to derive a simple model for linewidth evaluation when multiple sections biased differently are considered [101]. It is also possible that the absence of linewidth narrowing with increasing bias current observed in both DFB and DBR lasers may partly be induced by the surface gratings.

The SMSR and the peak emission wavelength variations with bias current have been extracted by feeding the laser output through a collimation setup to a single-mode optical fiber and measuring with an optical spectrum analyzer (OSA) with 10 pm spectral resolution. The bias current step was 5.2 mA and the heat sink temperature was 15 °C.

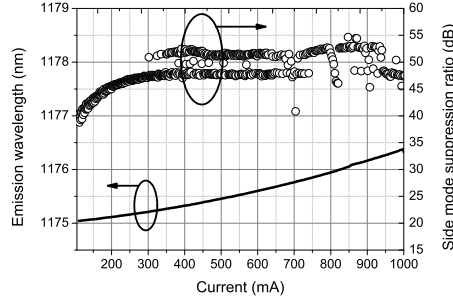


**Figure 6.9:** SMSR and emission wavelength variations with bias current for a 1180 nm DBR laser with 3<sup>rd</sup>-order ET-RWG surface gratings. [Pub2] reproduced with permission.

Figure 6.9 shows that the 1180 nm DBR lasers have good longitudinal mode discrimination with a SMSR over 40 dB from 200 mA to 1000 mA. Fluctuations in the SMSR are observed above 300 mA. They are associated with carrier and temperature induced changes of the material gain and refractive index as the bias current is varied. The emission wavelength current tuning rate is 1.4 pm mA<sup>-1</sup>.

The linewidth measurements point out that the re-broadening effects can have a significant effect on the emission linewidth and, combined with other limiting factors, they can limit the smallest attainable linewidth and prevent the typical  $1/P_0$  dependency of the linewidth. Due to re-broadening effects and to the dependencies of the output power and linewidth on the mirror losses and gain saturation, it is extremely challenging to obtain simultaneously a narrow emission linewidth and high output power.

**Table 6.1:** A comparison of the main characteristics between 1180 nm DBR lasers with 3<sup>rd</sup>-order ET-RWG gratings and 780 nm DFB lasers with 1<sup>st</sup>-order alternating and 3<sup>rd</sup>-order symmetrical LC-RWG gratings.

Characteristic	Alt. LC-RWG DFB	Sym. LC-RWG DFB	ET-RWG DBR
Wavelength (nm)	780	780	1180
Grating order	1	3	3
Power (mW)	40.9 at 300 mA	28.9 at 300 mA	497 at 1630 mA
Linewidth (kHz)	< 10	~ 10	100 < $\Delta\nu$ < 250
Slope efficiency per facet (W/A)	0.19	0.15	0.32
Threshold current density (kA/cm <sup>2</sup> )	1.566	2.358	0.712
Tuning rate (pm/mA)	5.1	5.5	1.4

Table 6.1 reveals a comparison between the measured 780 nm DFB lasers with LC-RWG gratings and the measured 1180 nm DBR lasers with ET-RWG gratings. It shows that the fabricated DFB lasers with 1<sup>st</sup>-order alternating and 3<sup>rd</sup>-order symmetrical gratings have much smaller emission linewidth, whereas the fabricated 1180 nm DBR lasers have better LI-characteristics. However, unlike in the 1180 nm DBR lasers, in which the output power of the DBR end facet is negligible, the AR-coated 780 nm DFB lasers have two output facets with similar power levels. Since the DBR lasers do not have gratings and lateral protrusions in the pumped gain section, the injection efficiency of the 1180 nm DBR lasers is likely better than the injection efficiency of the 780 nm DFB lasers with LC-RWG gratings. The better injection efficiency, asymmetric photon density distribution, and the wider and longer ridge of the pumped region contribute to the higher maximum output power of the DBR lasers. The DFB lasers are biased above the threshold current density over the entire length of the device. This decreases the linewidth of the DFB lasers compared to the DBR lasers as discussed in the previous chapters.

### 6.3 MOPA characterization results

The 780 nm DFB-MOPA threshold currents were first measured in MO DFB continuous wave (CW) mode and PA SOA pulsed mode with the devices mounted p-side-up. From those measurements it was determined that the threshold/transparency current of the PA SOA section was around 3 A. The 780 nm DFB-MOPA devices were then sent to an external company (Cavitar Oy) for p-side-down mounting and subsequently they were wire-bonded at ORC. The p-side-down mounted devices were then measured in CW mode for the MO DFB section and pulsed mode for the PA SOA section. The PA SOA pulsed mode results for the p-side down mounted devices were similar with the PA SOA pulsed mode results for the p-side-up mounted devices, because the heat generation is low in pulsed mode. The measurements have also shown that the gain peak of the PA SOA section and the emission/grating mode of the MO DFB section were detuned by several nm. The reason was that the MO DFB section was biased in CW mode and it experienced more heating than the PA SOA section, which was operated in pulsed mode. The CW operation of the MO DFB section also have an effect on the measured MOPA output power, since the CW output power of the MO DFB is smaller than in pulsed mode.

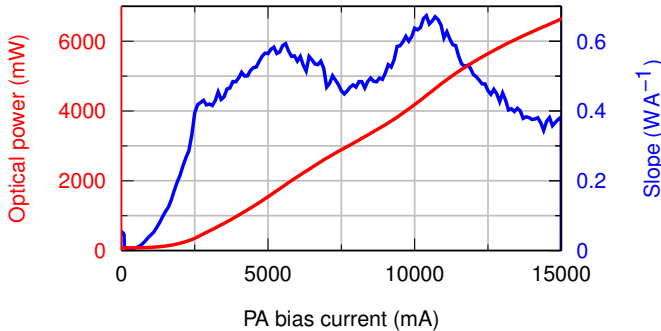


**Figure 6.10:** Light-current and slope efficiency characteristics for the PA SOA section of the 780 nm MOPA laser operated in pulsed mode with input from the MO DFB section operated in continuous wave mode.

Figure 6.10 shows a LI characteristic of a 780 nm MOPA device with a 3 mm long DFB

MO section and a 4 mm long tapered PA section operated in CW mode for the MO DFB section and in pulsed mode (1  $\mu$ s pulse width and 1% duty cycle) for the PA SOA section at 0 °C. The DFB section was biased with a 500 mA CW current. The full opening angle of the PA section was 6°. The output power reaches 7 W during the pulse, indicating that the devices can achieve a high output power with good thermal management. The 780 nm MOPA lasers were then driven in CW mode for both MO DFB and PA SOA sections and it was found that the PA SOA section does not produce amplification of the DFB power when biased above the 3 A threshold/transparency current determined in pulsed mode. From these measurements it was deduced that the thermal contact of the bonding was not adequate to achieve high-power lasing with the PA SOA section operated in CW mode. Accurate MOPA laser linewidth determination was not possible when operating the PA SOA section in pulsed mode. However, MOPA laser studies reported in the literature [102, 103] indicate that a linewidth broadening factor in the range from 5 to 10 could be expected after SOA amplification of a narrow linewidth moderate input power (5 mW to 15 mW) from a DFB MO section. Such a linewidth broadening factor would keep our MOPA linewidth below 100 kHz.



## 7 Conclusions

The application area of low cost narrow linewidth lasers that can generate a high output power while also having other desired properties, like a wide tuning range, good beam quality, small footprint, low power consumption and long device lifetime, is rapidly increasing. The thesis presents results of studies aimed at improving the characteristics of semiconductor lasers, which are the most promising solution for various applications requiring narrow linewidth emission at different wavelengths.

The results reported in the thesis show that the surface gratings can provide a cost effective alternative for buried gratings, which are conventionally used in high performance narrow linewidth lasers. The use of surface gratings eliminates the need for epitaxial regrowth, simplifying the fabrication, improving the device yield and reducing fabrication costs. The fabrication process is further simplified and made cost effective by employing UV-NIL in defining the etch masks. Also, with surface gratings, the defect-prone processed interfaces are kept away from the carrier flow and from regions with high optical field intensity and high temperature, reducing the degradation (and the associated characteristics' drift) and improving reliability. It was also demonstrated that, when properly designed, the surface gratings can achieve sufficient coupling coefficients to provide high SMSR stable single-mode operation with a good mode profile.

Surface gratings have been used less than buried gratings in edge emitting lasers because in many reported implementations they achieve lower coupling coefficients. This increases threshold currents and decreases the SMSR and the single mode operation stability. One reason for which the surface gratings' coupling coefficient is smaller is that the optical field is less confined in the grating areas of the surface gratings. However, the higher contrast in refractive index between the semiconductor grating regions and the grating trenches (containing the planarization material in our fabrication procedure) can compensate the small optical confinement in the surface grating area, especially when the grating is etched deep, close to the active region. Unfortunately, the etching depth is limited for narrow etching trenches because of the aspect ratio dependent etching (i.e. the maximum etching depth for which a good etching profile can be obtained is given by the technologically achievable aspect ratio between the etching depth and the grating trench width). The results reported in the thesis show that the LC-RWG grating trenches can be substantially widened by removing the lateral protrusions of the gratings alternately from opposite sides of the ridge, thus making the trenches even wider than the grating period. The wider trenches of alternating LC-RWG gratings enable the fabrication of lower order gratings with similar or higher coupling coefficients as those achieved by symmetric LC-RWG gratings fabricated under the same technological restrictions (i.e. with similar grating trench widths and etching aspect ratios). The alternating LC-RWG grating structures were employed in 1<sup>st</sup> order gratings for 780 nm DFB lasers and the fabricated devices were compared with DFB lasers fabricated from the same epiwafer with 3<sup>rd</sup> order symmetrical

gratings. The results indicated that the DFB lasers with alternating gratings had a higher spectral purity (i.e. broader range of high SMSR operation and narrower linewidths), lower threshold currents and higher slope efficiencies than the DFB lasers with symmetric gratings fabricated under the same technological restrictions. The laser characteristics were improved while the simulated coupling coefficients and the detuning factors for the two types of lasers were similar. Two mechanisms were identified as the reasons for these improvements. First, the radiation losses of the lower order gratings are smaller, which contributes to the better performance. Second, the total area of the protrusions, which act as lateral current leakage channels, was essentially halved. The use of the alternating gratings is especially relevant for short and visible wavelength lasers for which low order (particularly 1<sup>st</sup> order) LC-RWG gratings cannot be fabricated due to the etching aspect ratio limits.

The device fabrication method described in the thesis, employing UV-NIL to define the etch mask patterns for the surface gratings, has various advantages as compared to other methods that are used to fabricate edge-emitting DFB and DBR lasers. The UV-NIL-based high-resolution mechanical pattern replication technique significantly lowers the fabrication costs, increases the throughput and improves the device fabrication yield while enabling the realization of irregular non-periodic patterns. The advantages and the disadvantages of the device fabrication method were identified and the technological limitations in the fabrication of lasers with surface gratings were discussed in the thesis.

The theory of laser diode emission was used to analyze the effects of different structural parameters on the device characteristics, particularly on the emission linewidth. By following the guidelines derived from theoretical analysis and simulation results, the fabricated lasers achieved state-of-the-art characteristics: 0.5 W output power with >45–50 dB SMSR and 125 kHz to 250 kHz linewidth FWHM for DBR lasers; 30 mW to 40 mW output powers with ~50 dB SMSR and ~10 kHz linewidth for DFB lasers. These characteristics have been obtained despite the fact that the surface structures and their fabrication technology are not mature.

A major challenge was to achieve simultaneously a high output power and a narrow emission linewidth. These characteristics are contradictory coupled through multiple structural parameters of the lasers and certain combination ranges of output power and narrow linewidth cannot be achieved with a single cavity DFB or DBR laser. Consequently, in order to achieve simultaneously a very narrow emission linewidth and a high W-level output power, a tapered semiconductor optical amplifier was integrated with a DFB laser in a MOPA structure. The monolithically integrated PA SOA section boosts up the narrow linewidth injection from the MO DFB section, for achieving high-power narrow-linewidth operation in a highly compact, easily integrable and mechanically robust low cost laser source. The MOPA device structure also enables the independent control of the emission wavelength and of the output power through separate bias currents for the MO DFB and for the PA SOA sections. The fabricated MOPA lasers achieved a high ~7 W output power in pulsed mode for the SOA PA section but they did not lase in CW mode for the SOA PA section due to p-side down mounting alignment difficulties and poor thermal management. Improved mounting and thermal management (particularly by a better thermal contact between the p-side contact layer and the AlN submount) are expected to enable CW MOPA lasing.

Besides the cost-effective fabrication method and state-of-the-art narrow emission linewidth and high output power, the monolithical robustness and the small size are also significant advantages of the developed devices. These features are vital for a whole range of appli-

cations, including chip scale low cost frequency standards [104], optical communications [105], spectroscopy [106], and medical applications [107].

The future research should aim to improve the device yield, output powers and wall-plug efficiencies for the 780 nm DFB and 1180 nm DBR lasers.

Due to the relatively large area of the lateral protrusions, the LC-RWG DFB lasers suffer from a large lateral current leakage which has a negative effect on the device heating, on the threshold current and on the slope efficiency, limiting the saturated output power and wall-plug efficiency. Although some reduction of this current leakage is achieved by employing LC-RWG gratings with alternating lateral protrusions, the possibility to eliminate the lateral current leakage through the protrusions by employing oxidized apertures should be investigated in the future.

Improved SOA PA section structures, better p-side down mounting and improved thermal management should be developed in order to combine the narrow linewidth injection of the DFB MO with the demonstrated amplification capability of the monolithically-integrated SOA in order to achieve CW high-power ( $>1$  W) narrow linewidth DFB MOPA laser emission. The CW operation will allow MOPA laser linewidth measurements and experimental analysis of the linewidth broadening induced by the amplification in a monolithically integrated SOA section. The use of a tapered RWG gain section and tilted placement on chip should also be tested to investigate the possibilities to further increase the output power level and to reduce the emission linewidth in the DBR lasers with ET-RWG gratings.





## 8 Appendix A

**Table 8.1:** Simulation parameters for the DFB lasers emitting at 780 nm. [Pub1] reproduced with permission.

symbol	parameter	value
$\lambda_0$	emission wavelength	780 nm
$n_{eff,0}$	effective refractive index	3.35
$n_g$	group index	4.0
$W$	ridge width	2 $\mu\text{m}$
$d$	thickness of the guiding area	0.2 $\mu\text{m}$
$\Gamma$	optical confinement factor	0.025
$\alpha_i$	internal loss factor	12 $\text{cm}^{-1}$
$A$	monomolecular recombination coefficient	0 $\text{s}^{-1}$
$B$	bimolecular recombination coefficient	$1 \times 10^{-10} \text{ cm}^3 \text{ s}^{-1}$
$C$	Auger recombination coefficient	$3 \times 10^{-29} \text{ cm}^6 \text{ s}^{-1}$
$N_{tr}$	transparency carrier density	$3.47 \times 10^{18} \text{ cm}^{-3}$
$\frac{\partial g_m}{\partial N}$	differential gain	$4.5 \times 10^{-16} \text{ cm}^2$
$\alpha_{H,eff}$	effective linewidth enhancement factor	4.0
$n_{sp}$	population inversion factor	2
$\beta$	spontaneous emission coupling factor	$2.8705 \times 10^{-6}$
$\eta_i$	internal quantum efficiency	0.5
$\epsilon$	gain compression factor	$1.0 \times 10^{-17} \text{ cm}^3$
$K_c$	Petermann factor	1
$J$	injection current density	6.25 $\text{kA/cm}^2$



# Bibliography

- [1] H. Jelinkova, *Lasers For Medical Applications : Diagnostics, Therapy And Surgery*. Elsevier Science, 2013.
- [2] B. C. Barish and R. Weiss, “LIGO and the Detection of Gravitational Waves,” *Physics Today*, vol. 52, no. 10, pp. 44–50, 1999.
- [3] T. Schneider, “Ultrahigh-Bitrate Wireless Data Communications via THz-Links; Possibilities and Challenges,” *Journal of Infrared, Millimeter, and Terahertz Waves*, vol. 36, no. 2, pp. 159–179, 2015.
- [4] C. Affolderbach, F. Droz, and G. Mileti, “Experimental demonstration of a compact and high-performance laser-pumped rubidium gas cell atomic frequency standard,” *IEEE Transactions on Instrumentation and Measurement*, vol. 55, no. 2, pp. 429–435, 2006.
- [5] A. J. McGettrick, W. Johnstone, R. Cunningham, and J. D. Black, “Tunable diode laser spectroscopy with wavelength modulation: Calibration-free measurement of gas compositions at elevated temperatures and varying pressure,” *Journal of Lightwave Technology*, vol. 27, no. 15, pp. 3150–3161, 2009.
- [6] J. C. Bergquist, R. G. Hulet, W. M. Itano, and D. J. Wineland, “Observation of Quantum Jumps in a Single Atom,” *Physical Review Letters*, vol. 57, no. 14, pp. 1699–1702, 1986.
- [7] C. Oates, F. Bondu, R. Fox, and L. Hollberg, “A diode-laser optical frequency standard based on laser-cooled Ca atoms: Sub-kilohertz spectroscopy by optical shelving detection,” *The European Physical Journal D*, vol. 7, no. 3, pp. 449–460, 1999.
- [8] K. Numata, J. Camp, M. A. Krainak, and L. Stolpner, “Performance of planar-waveguide external cavity laser for precision measurements,” *Optics Express*, vol. 18, no. 22, pp. 22 781–22 788, 2010.
- [9] C. Henry, “Theory of the linewidth of semiconductor lasers,” *IEEE Journal of Quantum Electronics*, vol. 18, no. 2, pp. 259–264, 1982.
- [10] R. Engelbrecht, B. Lins, P. Zinn, R. Buchtal, and B. Schmauss, “Line shapes of near-infrared DFB and VCSEL diode lasers under the influence of system back reflections,” *Applied Physics B*, vol. 109, no. 3, pp. 441–452, 2012.
- [11] M. Okai, M. Suzuki, and T. Taniwatari, “Strained multiquantum-well corrugation-pitch-modulated distributed feedback laser with ultranarrow (3.6 kHz) spectral linewidth,” *Electronics Letters*, vol. 29, no. 19, pp. 1696–1697, 1993.

- [12] J. W. Zimmerman, R. K. Price, U. Reddy, N. L. Dias, and J. J. Coleman, "Narrow Linewidth Surface-Etched DBR Lasers: Fundamental Design Aspects and Applications," *IEEE Journal of Selected Topics in Quantum Electronics*, vol. 19, no. 4, pp. 1 503 712–1 503 712, 2013.
- [13] S. Perrin, F. Esnault, and D. Holleville, "A new design of ECLD for compact atomic clocks," in *IEEE International Frequency Control Symposium, 2007 Joint with the 21st European Frequency and Time Forum*. IEEE, 2007, pp. 86–89.
- [14] S. Peil, S. Crane, and T. Swanson, "Rubidium-fountain characterization using the USNO clock ensemble," in *IEEE International Frequency Control Symposium, 2007 Joint with the 21st European Frequency and Time Forum*. IEEE, 2007, pp. 473–476.
- [15] E. Ip, A. P. T. Lau, D. J. F. Barros, and J. M. Kahn, "Coherent detection in optical fiber systems," *Optics Express*, vol. 16, no. 2, p. 753, 2008.
- [16] R. Phelan, J. O'Carroll, D. Bryne, R. Lennox, K. Carney, L. P. Barry, and B. Kelly, "Low linewidth discrete mode lasers for coherent communications applications," in *2014 The European Conference on Optical Communication (ECOC)*. IEEE, 9 2014, pp. 1–3.
- [17] J. Senior and M. Jamro, *Optical fiber communications: principles and practice*. Pearson Education, 2009.
- [18] S. Kraft, A. Deninger, C. Trück, and J. Fortágh, "Rubidium spectroscopy at 778–780 nm with a distributed feedback laser diode," *Laser Physics*, vol. 2, no. 2, p. 71, 2004.
- [19] A. Klehr, H. Wenzel, O. Brox, F. Bugge, and G. Erbert, "High power DFB lasers for D1 and D2 caesium absorption spectroscopy and atomic clocks," in *Proc. of SPIE*, vol. 6909. SPIE, 2008, pp. 69 091E–1.
- [20] A. Klehr, H. Wenzel, O. Brox, and F. Bugge, "High power DFB lasers for D1 and D2 rubidium absorption spectroscopy and atomic clocks," *Proc. of SPIE*, vol. 7230, p. 72301I, 2009.
- [21] K. Gbele, A. Laurain, J. Hader, and W. Stolz, "Design and fabrication of hybrid metal semiconductor mirror for high-power VECSEL," *IEEE Photonics Technology Letters*, vol. 28, no. 7, pp. 732–735, 2016.
- [22] K. Renk, "Basics of laser physics." Springer Berlin Heidelberg, 2012, ch. 3.
- [23] J. Huang, "Design-in reliability for modern wavelength-division multiplex (WDM) distributed feedback (DFB) InP lasers," *Applied Physics Research*, vol. 4, no. 2, p. 15, 2012.
- [24] S. J. Jang, J. S. Yu, and Y. T. Lee, "Laterally Coupled DFB Lasers With Self-Aligned Metal Surface Grating by Holographic Lithography," *IEEE Photonics Technology Letters*, vol. 20, no. 7, pp. 514–516, 2008.
- [25] J. Viheriälä, T. Niemi, J. Kontio, and M. Pessa, "Nanoimprint lithography-next generation nanopatterning methods for nanophotonics fabrication," in *Recent Optical and Photonic Technologies*. InTech, 2010.

- [26] J. Li and J. Cheng, "A laterally-coupled distributed feedback laser with equivalent quarter-wave phase shift," *Optics Express*, Vol. 21, Issue 22, pp. 26936-26941, vol. 21, no. 22, pp. 26 936–26 941, 2013.
- [27] C. Vieu, F. Carcenac, A. Pépin, Y. Chen, M. Mejias, A. Lebib, L. Manin-Ferlazzo, L. Couraud, and H. Launois, "Electron beam lithography: resolution limits and applications," *Applied Surface Science*, vol. 164, no. 1, pp. 111–117, 2000.
- [28] D. Dougherty, R. Muller, and P. Maker, "Stitching-error reduction in gratings by shot-shifted electron-beam lithography," *Journal of lightwave technology*, vol. 19, no. 10, p. 1527, 2001.
- [29] M. Esashi, A. Kojima, and N. Ikegami, "Development of massively parallel electron beam direct write lithography using active-matrix nanocrystalline-silicon electron emitter arrays," *Microsystems & Nanoengineering*, vol. 1, p. 15029, 2015.
- [30] A. Wong, *Resolution enhancement techniques in optical lithography*, 47th ed. SPIE press, 2001.
- [31] Z. Cui, *Nanofabrication : principles, capabilities and limits*, 2nd ed. Springer, 2008.
- [32] D. Z. Pan, J.-s. Yang, K. Yuan, M. Cho, and Y. Ban, "Layout optimizations for double patterning lithography," in *2009 IEEE 8th International Conference on ASIC*. IEEE, 2009, pp. 726–729.
- [33] J. Li and J. Cheng, "A laterally-coupled distributed feedback laser with equivalent quarter-wave phase shift," *Optics Express*, vol. 21, no. 22, p. 26936, 2013.
- [34] S. Chou, P. Krauss, and P. Renstrom, "Imprint of sub-25 nm vias and trenches in polymers," *Applied physics letters*, vol. 67, no. 21, pp. 3114–3116, 1995.
- [35] G. Kreindl, M. Kast, and D. Treiblmary, "Soft UV-NIL at the 12.5 nm Scale," *Proc SPIE*, vol. 7970, pp. 79 701M–2, 2011.
- [36] H. Lan and H. Liu, "UV-Nanoimprint Lithography: Structure, Materials and Fabrication of Flexible Molds," *Journal of Nanoscience and Nanotechnology*, vol. 13, no. 5, pp. 3145–3172, 2013.
- [37] N. Li, W. Wu, and S. Chou, "Sub-20-nm alignment in nanoimprint lithography using Moire fringe," *Nano Letters*, vol. 6, no. 11, pp. 2626–2629, 2006.
- [38] A. d. Campo and E. Arzt, *Generating micro-and nanopatterns on polymeric materials*. John Wiley & Sons, 2011.
- [39] J. Viheriälä, J. Tommila, T. Leinonen, M. Dumitrescu, L. Toikkanen, T. Niemi, and M. Pessa, "Applications of UV-nanoimprint soft stamps in fabrication of single-frequency diode lasers," *Microelectronic Engineering*, vol. 86, no. 3, pp. 321–324, 2009.
- [40] H. Schmitt, M. Zeidler, M. Rommel, A. Bauer, and H. Ryssel, "Custom-specific UV nanoimprint templates and life-time of antisticking layers," *Microelectronic Engineering*, vol. 85, no. 5-6, pp. 897–901, 2008.

- [41] M. Lax, "Classical noise. V. Noise in self-sustained oscillators," *Physical Review*, vol. 160, no. 2, p. 290, 1967.
- [42] G. Duan and P. Gallion, "Drive current noise induced linewidth in tunable multielectrode lasers," *IEEE Photonics Technology Letters*, vol. 3, no. 4, pp. 302–304, 1991.
- [43] G. D. Domenico, S. Schilt, and P. Thomann, "Simple approach to the relation between laser frequency noise and laser line shape," *Applied Optics*, vol. 49, no. 25, pp. 4801–4807, 2010.
- [44] H. Zhou, X. Yuan, and X. Ma, "Randomness generation based on spontaneous emissions of lasers," *Physical Review A*, vol. 91, no. 6, p. 062316, 2015.
- [45] W. Tsang, *Lightwave Communications Technology*. Academic Press, 1985, vol. 22.
- [46] M. Fleming and A. Mooradian, "Fundamental line broadening of single-mode (GaAl) As diode lasers," *Applied Physics Letters*, vol. 38, no. 7, pp. 511–513, 1981.
- [47] J. Ehrhardt, A. Villeneuve, and G. Stegeman, "Interferometric measurement of the linewidth enhancement factor of a 1.55- $\mu\text{m}$  strained multiquantum-well InGaAs/InGaAsP amplifier," *IEEE Photonics Technology Letters*, vol. 4, no. 12, pp. 1335–1338, 1992.
- [48] H. Li, "RF-modulation measurement of linewidth enhancement factor and nonlinear gain of vertical-cavity surface-emitting lasers," *IEEE Photonics Technology Letters*, vol. 8, no. 12, pp. 1594–1596, 1996.
- [49] K. Iiyama, K. Hayashi, and Y. Ida, "Simple method for measuring the linewidth enhancement factor of semiconductor lasers by optical injection locking," *Optics Letters*, vol. 17, no. 16, pp. 1128–1130, 1992.
- [50] T. Newell, D. Bossert, A. Stintz, and B. Fuchs, "Gain and linewidth enhancement factor in InAs quantum-dot laser diodes," *IEEE Photonics Technology Letters*, vol. 11, no. 12, pp. 1527–1529, 1999.
- [51] G. Agrawal and C. Bowden, "Concept of linewidth enhancement factor in semiconductor lasers: its usefulness and limitations," *IEEE Photonics Technology Letters*, vol. 5, no. 6, pp. 640–642, 1993.
- [52] G. Liu, X. Jin, and S. Chuang, "Measurement of linewidth enhancement factor of semiconductor lasers using an injection-locking technique," *IEEE Photonics Technology Letters*, vol. 13, no. 5, pp. 430–432, 2001.
- [53] L. Coldren, S. Corzine, and M. Mashanovitch, *Diode lasers and photonic integrated circuits*, 2nd ed. John Wiley & Sons, 2012.
- [54] J. Wang, N. Schunk, and K. Petermann, "Linewidth enhancement for DFB lasers due to longitudinal field dependence in the laser cavity," *Electronics Letters*, vol. 23, no. 14, pp. 715–717, 1987.
- [55] K. Petermann, *Laser diode modulation and noise*, 3rd ed. Springer Science & Business Media, 2012.

- [56] T. Yamanaka, Y. Yoshikuni, and K. Yokoyama, "Theoretical study on enhanced differential gain and extremely reduced linewidth enhancement factor in quantum-well lasers," *IEEE Journal of Quantum Electronics*, vol. 29, no. 6, pp. 1609–1616, 1993.
- [57] A. Aiello, M. V. Exter, and G. Nienhuis, "Does excess quantum noise exist in spontaneous processes?" *Optics Communications*, vol. 213, no. 1, pp. 81–87, 2002.
- [58] M. Newstein, "The spontaneous emission factor for lasers with gain induced waveguiding," *IEEE Journal of Quantum Electronics*, vol. 20, no. 11, pp. 1270–1276, 1984.
- [59] H. Yasaka, M. Fukuda, and T. Ikegami, "Current tailoring for lowering linewidth floor (semiconductor lasers)," *Electronics Letters*, vol. 24, no. 12, pp. 760–762, 1988.
- [60] M. Fukuda, *Optical semiconductor devices*. John Wiley & Sons, 1999.
- [61] G. Smith, J. Hughes, R. Lammert, M. Osowski, G. Papen, J. Verdeyen, and J. Coleman, "Very narrow linewidth asymmetric cladding InGaAs-GaAs ridge waveguide distributed Bragg reflector lasers," *IEEE Photonics Technology Letters*, vol. 8, no. 4, pp. 476–478, 1996.
- [62] A. L. Schawlow and C. H. Townes, "Infrared and Optical Masers," *Physical Review*, vol. 112, no. 6, pp. 1940–1949, 1958.
- [63] G. Morthier and P. Vankwikelberge, *Handbook of distributed feedback laser diodes*. Artech House, 2013.
- [64] K. Kikuchi, "Origin of residual semiconductor-laser linewidth in high-power limit," *Electronics Letters*, vol. 24, no. 16, pp. 1001–1002, 1988.
- [65] M. O'Mahony and I. Henning, "Semiconductor laser linewidth broadening due to  $1/f$  carrier noise," *Electronics Letters*, vol. 19, no. 23, pp. 1000–1001, 1983.
- [66] H. Wenzel, H. Wunsche, and U. Bandelow, "Linewidth rebroadening in semiconductor lasers due to lateral spatial holeburning," *Electronics Letters*, vol. 27, no. 25, pp. 2301–2302, 1991.
- [67] K. Takaki, T. Kise, and K. Maruyama, "Reduced linewidth re-broadening by suppressing longitudinal spatial hole burning in high-power 1.55- $\mu\text{m}$  continuous-wave distributed-feedback (CW-DFB)," *IEEE Journal of Quantum Electronics*, vol. 39, no. 9, pp. 1060–1065, 2003.
- [68] X. Pan, B. Tromborg, and H. Olesen, "Linewidth rebroadening in DFB lasers due to weak side modes," *IEEE Photonics Technology Letters*, vol. 3, no. 2, pp. 112–114, 1991.
- [69] F. Girardin, G. Duan, and P. Gallion, "Linewidth rebroadening due to nonlinear gain and index induced by carrier heating in strained quantum-well lasers," *IEEE Photonics Technology Letters*, vol. 8, no. 3, pp. 334–336, 1996.
- [70] H. Olesen, B. Tromborg, H. Lassen, and X. Pan, "Mode instability and linewidth rebroadening in DFB lasers," *Electronics Letters*, vol. 28, no. 5, pp. 444–446, 1992.



- [71] H. Yamazaki and M. Yamaguchi, "Spectral linewidth rebroadening in MQW-DFB LDs caused by spontaneous emission noise in SCH/barrier layers," *IEEE Photonics Technology Letters*, vol. 6, no. 3, pp. 341–343, 1994.
- [72] W. Burkett, B. Lu, and M. Xiao, "Influence of injection-current noise on the spectral characteristics of semiconductor lasers," *IEEE Journal of Quantum Electronics*, vol. 33, no. 11, pp. 2111–2118, 1997.
- [73] F. Kano, Y. Tohmori, Y. Kondo, and M. Nakao, "Spectral linewidth reduction (580 kHz) in structure-optimised 1.5  $\mu\text{m}$  butt-jointed distributed Bragg reflector lasers," *Electronics Letters*, vol. 25, no. 11, pp. 709–710, 1989.
- [74] B. Zhao, T. Chen, and A. Yariv, "A comparison of amplitude-phase coupling and linewidth enhancement in semiconductor quantum-well and bulk lasers," *IEEE Journal of Quantum Electronics*, vol. 29, no. 4, pp. 1027–1030, 1993.
- [75] Y. Arakawa and H. Sakaki, "Multidimensional quantum well laser and temperature dependence of its threshold current," *Applied Physics Letters*, vol. 40, no. 11, pp. 939–941, 1982.
- [76] M. Asada, Y. Miyamoto, and Y. Suematsu, "Gain and the threshold of three-dimensional quantum-box lasers," *IEEE Journal of Quantum Electronics*, vol. 22, no. 9, pp. 1915–1921, 1986.
- [77] A. Adams, "Strained-layer quantum-well lasers," *IEEE Journal of Selected Topics in Quantum Electronics*, vol. 17, no. 5, pp. 1364–1373, 2011.
- [78] Y. Arakawa and A. Yariv, "Theory of gain, modulation response, and spectral linewidth in AlGaAs quantum well lasers," *IEEE Journal of Quantum Electronics*, vol. 21, no. 10, pp. 1666–1674, 1985.
- [79] A. Ghitii, E. O'Reilly, and A. Adams, "Improved dynamics and linewidth enhancement factor in strained-layer lasers," *Electronics Letters*, vol. 25, no. 13, pp. 821–823, 1989.
- [80] T. Uusitalo, H. Virtanen, and M. Dumitrescu, "Transverse structure optimization of distributed feedback and distributed Bragg reflector lasers with surface gratings," *Optical and Quantum Electronics*, vol. 49, no. 6, p. 206, 2017.
- [81] O. Brox, F. Bugge, and A. Mogilatenko, "Distributed feedback lasers in the 760 to 810 nm range and epitaxial grating design," *Semiconductor Science and Technology*, vol. 29, no. 9, p. 095018, 2014.
- [82] D. Fang, Y. Zhang, C. Li, C. Manzaneda, and B. Li, "Effect of DBR geometry on reflectivity and spectral linewidth of DBR lasers." *Bandaoti Xuebao(Chinese Journal of Semiconductors)*, vol. 26, no. 12, pp. 2315–2319, 2005.
- [83] D. Anderson and N. Apsley, "The Hall effect in III-V semiconductor assessment," *Semiconductor Science and Technology*, vol. 1, no. 3, p. 187, 1986.
- [84] T. Ronnie, "Advances in high-power laser diode packaging," in *Semiconductor Laser Diode Technology and Applications*. InTech, 2012.

- [85] J. Coburn and H. Winters, "Ion- and electron-assisted gas-surface chemistry—An important effect in plasma etching," *Journal of Applied physics*, vol. 50, no. 5, pp. 3189–3196, 1979.
- [86] J. Yeom, Y. Wu, J. C. Selby, and M. A. Shannon, "Maximum achievable aspect ratio in deep reactive ion etching of silicon due to aspect ratio dependent transport and the microloading effect," *Journal of Vacuum Science & Technology B: Microelectronics and Nanometer Structures*, vol. 23, no. 6, p. 2319, 2005.
- [87] R. Gottscho and C. Jurgensen, "Microscopic uniformity in plasma etching," *Journal of Vacuum Science & Technology B: Microelectronics and Nanometer Structures Processing, Measurement, and Phenomena*, vol. 10, no. 5, pp. 2133–2147, 1992.
- [88] C. Hedlund, H. Blom, and S. Berg, "Microloading effect in reactive ion etching," *Journal of Vacuum Science & Technology A: Vacuum, Surfaces, and Films*, vol. 12, no. 4, pp. 1962–1965, 1994.
- [89] J. W. Coburn and H. F. Winters, "Conductance considerations in the reactive ion etching of high aspect ratio features," *Applied Physics Letters*, vol. 55, no. 26, pp. 2730–2732, 1989.
- [90] C. Wang and B. Abraham-Shrauner, "Effect of shadowing ion energy flux and neutral flux and isotropic neutral flux on plasma etching profiles," in *University/Government/Industry Microelectronics Symposium, 1997., Proceedings of the Twelfth Biennial*. IEEE, 1997, p. 123.
- [91] J. Arnold and H. Sawin, "Charging of pattern features during plasma etching," *Journal of Applied Physics*, vol. 70, no. 10, pp. 5314–5317, 1991.
- [92] W. Park, J. Kim, S. Cho, S. Yoon, S. Suh, and D. Yoon, "High aspect ratio via etching conditions for deep trench of silicon," *Surface and Coatings Technology*, vol. 171, no. 1, pp. 290–295, 2003.
- [93] C. Chung, H. Lu, and T. Jaw, "High aspect ratio silicon trench fabrication by inductively coupled plasma," *Microsystem Technologies*, vol. 6, no. 3, pp. 106–108, 2000.
- [94] K. Owen and B. VanDerElzen, "High aspect ratio deep silicon etching," in *2012 IEEE 25th International Conference on Micro Electro Mechanical Systems (MEMS)*. IEEE, 2012, pp. 251–254.
- [95] W. Streifer, R. Burnham, and D. Scifres, "Radiation losses in distributed feedback lasers and longitudinal mode selection," *IEEE Journal of Quantum Electronics*, vol. 12, no. 11, pp. 737–739, 1976.
- [96] J. Mark, E. Bødtker, and B. Tromborg, "Measurement of Rayleigh backscatter-induced linewidth reduction," *Electronics Letters*, vol. 21, no. 22, pp. 1008–1009, 1985.
- [97] L. Richter, H. Mandelberg, and M. Kruger, "Linewidth determination from self-heterodyne measurements with subcoherence delay times," *IEEE Journal of Quantum Electronics*, vol. 22, no. 11, pp. 2070–2074, 1986.
- [98] L. Mercer, "1/f frequency noise effects on self-heterodyne linewidth measurements," *Journal of Lightwave Technology*, vol. 9, no. 4, pp. 485–493, 1991.

- [99] S. Huang, T. Zhu, M. Liu, and W. Huang, "Precise measurement of ultra-narrow laser linewidths using the strong coherent envelope," *Scientific Reports*, vol. 7, p. 41988, 2017.
- [100] S. Spießberger, M. Schiemangk, A. Wicht, H. Wenzel, G. Erbert, and G. Tränkle, "DBR laser diodes emitting near 1064 nm with a narrow intrinsic linewidth of 2 kHz," *Applied Physics B*, vol. 104, no. 4, pp. 813–818, 2011.
- [101] B. Tromborg, H. Olesen, and X. Pan, "Theory of linewidth for multielectrode laser diodes with spatially distributed noise sources," *IEEE Journal of Quantum Electronics*, vol. 27, no. 2, pp. 178–192, 1991.
- [102] A. Champagne, J. Camel, R. Maciejko, K. Kasunic, D. Adams, and B. Tromborg, "Linewidth broadening in a distributed feedback laser integrated with a semiconductor optical amplifier," *IEEE Journal of Quantum Electronics*, vol. 38, no. 11, pp. 1493–1502, 2002.
- [103] M. V. Suárez, M. Krakowski, Y. Robert, and E. Vinet, "Monolithic master oscillator power amplifier at 1.58  $\mu\text{m}$  for lidar measurements," in *International Conference on Space Optics (ICSO 2014)*. E.T.S.I. Telecomunicación (UPM), 2014, pp. 1–8.
- [104] M. Violetti, C. Affolderbach, and F. Merli, "Miniaturized microwave cavity for rubidium atomic frequency standards," in *2012 7th European Microwave Integrated Circuits Conference (EuMIC)*. IEEE, 2012, pp. 940–943.
- [105] J. O'Carroll, R. Phelan, B. Kelly, and T. Huynh, "Narrow-linewidth discrete-mode laser diodes for coherent communication applications," *Journal of Optical Communications and Networking*, vol. 4, no. 9, pp. A90–A96, 2012.
- [106] A. Cygan, D. Lisak, P. Morzyński, and M. Bober, "Cavity mode-width spectroscopy with widely tunable ultra narrow laser," *Optics Express*, vol. 21, no. 24, pp. 29 744–29 754, 2013.
- [107] A. Müller, S. Marschall, and O. Jensen, "Diode laser based light sources for biomedical applications," *Laser & Photonics Reviews*, vol. 7, no. 5, pp. 605–627, 2013.

# Publications



# Publication I

Optical and Quantum Electronics, "Simulation studies of DFB laser longitudinal structures for narrow linewidth emission", vol. 49, 2017, p. 160, H. Virtanen, T. Uusitalo, and M. Dumitrescu,

© Springer Science+Business Media New York 2017 with permission of Springer. The final publication is available at Springer via

<https://doi.org/10.1007/s11082-017-0993-8>



# Publication II

©2017 IEEE. Reprinted, with permission, from H. Virtanen, A. T. Aho, J. Viheriälä, V.M. Korpjarvi, T. Uusitalo, M. Koskinen, M. Dumitrescu, and M. Guina, "Spectral characteristics of narrow linewidth high-power 1180 nm DBR laser with surface gratings", IEEE Photonics Technology Letters, Jan. 2017





# Publication III

H. Virtanen, T. Uusitalo, M. Karjalainen, S. Ranta, J. Viheriälä, V.M. Korpijärvi, and M. Dumitrescu, "Narrow-linewidth 780 nm DFB laser fabricated using nanoimprint lithography", *IEEE Photonics Technology Letters* - Approved



# Publication IV

T. Uusitalo, H. Virtanen, M. Karjalainen, S. Ranta, J. Viheriälä, V.M. Korpijarvi, and M. Dumitrescu, "Distributed feedback lasers with alternating laterally-coupled ridge-waveguide surface gratings", *Optics Letters*, vol. 42, no. 16, pp. 3141–3144, 2017.

<https://doi.org/10.1364/OL.42.003141>

© 2017. Optical Society of America. One print or electronic copy may be made for personal use only. Systematic reproduction and distribution, duplication of any material in this paper for a fee or for commercial purposes, or modifications of the content of this paper are prohibited.

Tampereen teknillinen yliopisto  
PL 527  
33101 Tampere

Tampere University of Technology  
P.O.B. 527  
FI-33101 Tampere, Finland

ISBN 978-952-15-4048-6  
ISSN 1459-2045